Bringing Back the Senses to LUX-ZEPLIN



Anthony Swain

Lincoln College

University of Oxford

A thesis presented for the degree of

Master of Science by Research

Abstract

The LUX-ZEPLIN (LZ) experiment set world-leading limits for spin-independent WIMP-nucleon interactions above 10 GeV/c^2 with its first science run results released in 2022. Background characterisation and a complete understanding of the detector and internal conditions are vital to achieve and improve upon such limits; in the chance of discovery, these are a necessity to provide a foundation for the result. LZ utilizes a dual-phase time projection chamber (TPC) with 7 tonnes of active Xenon to generate and image signals within the detector. Acoustic sensors; loop antennae; and weir-level sensors were developed and installed on the detector to monitor the vibrational and electromagnetic environments as well as detect the presence of any surface waves within the TPC. This thesis presents the first studies into monitoring the internal conditions of the LZ TPC using these sensors' on-event data, showing that they fulfill their design purpose. Additionally, this thesis starts to answer the collaboration's biggest questions of what can be seen in the sensors and attempts to link signals observed in the sensors to pathologies observed in PMT data.

Contents

1 Dark Matter **9**

1.1 Evidence for Dark Matter . . . 10

1.1.1 Velocity Dispersion . . . 10

1.1.2 Weak Gravitational Lensing & The Bullet Cluster . . . 11

1.1.3 The Cosmic Microwave Background . . . 12

1.1.4 The ΛCDM Model . . . 14

1.2 Dark Matter Candidates . . . 15

1.2.1 WIMPs . . . 15

1.2.2 Neutrinos . . . 16

1.2.3 Axions . . . 16

2 The LUX-ZEPLIN Experiment **18**

2.1 Overview . . . 18

2.1.1 2022 Sensitivity Result . . . 18

2.1.2 Detector Overview . . . 19

2.2 The Time Projection Chamber . . . 19

2.2.1 High-Voltage Grids . . . 24

2.3 The Veto Detectors & Water Tank . . . 25

2.4 Xenon Circulation and Purification . . . 26

2.5 Internal Monitoring Sensors . . . 27

2.5.1 Acoustic Sensors . . . 29

2.5.2 Loop Antenna . . . 31

2.5.3 Weir Precision Sensors . . . 34

3 Fast Sensor Analysis Framework **38**

4 Results **41**

4.1 Solenoid Valve Actuations . . . 41

4.2 Weir Precision Sensors . . . 46

4.3 Hotspots . . . 52

4.4 LZ as a Seismometer . . . 54

4.5 PMT-Trips . . . 56

4.6 Conclusion . . . 56

5 Outlook **59**

List of Figures

1 Rotational curve of galaxy NGC 2903 with a dark-halo fit. The dashed line shows the visible matter contribution; the dotted line shows the gas contribution and; the dot dashed line shows the contribution from the Dark Matter halo. Figure taken from [1]. 11

2 False colour image of the bullet cluster. Pink shows the region of hot gas, containing most of the visible matter the clusters. Blue shows the regions where most the mass is found using weak gravitational lensing. Image credit: X-ray: NASA/CXC/M.Markevitch et al. Optical: NASA/STScI; Magellan/U.Arizona/D.Clowe et al. Lensing Map: NASA/STScI; ESO WFI; Magellan/U.Arizona/D.Clowe et al. 12

3 Angular power spectrum of the CMB, measured by the Planck collaboration, 2018. Figure taken from [2]. 14

4 Overview of hypothesised Dark Matter candidates over 51 orders of mass range; split into wave-like and particle-like candidates. Figure taken from [3]. 15

5 LUX-ZEPLIN's 2022 sensitivity result with 60-live days of data taking; published in 2023. The 90% confidence limit for the spin independent WIMP cross section vs. WIMP mass is shown by the black line. The green and yellow bands are the 1σ and 2σ sensitivity bands respectively. The dotted line shows the median of the sensitivity projection. Limits are also shown from the PandaX-4T [4], XenonNT [5], LUX [6] and DEAP-3600 [7] experiments. Plot from the LUX-ZEPLIN SR1 results paper [8]. 18

6 Visualization of the LZ detector in BACCARAT (Basically, A Component-Centric. Analog Response to AnyThing - an LZ simulation package built on GEANT4). The TPC (magenta) within the cryostat (light green) is surrounded by the GdLS outer detector tanks (yellow) that are immersed in a water tank. The inner part of the water tank within the PMT structure is shown in blue. Figure and caption taken from [9]. 20

7 Operating principle of the dual phase Xe TPC. Particle interactions in the liquid Xenon (LXe) produce two energy signatures; scintillation photons (S1) and electrons which are drifted by a vertical electric field into the gaseous phase of the Xe and are observed as electroluminescence (S2). The LXe surface lies between the anode grid and gate grids as shown by the pink outline with the gaseous phase lying above. The PMTs are located above and below the anode grid and bottom grid respectively. Note: The shown applied voltages are varied between science runs to meet the needs of the experiment. 21

8 Calibration events used in SR1 plotted as $\log_{10}$S2c-S1c for the tritum source (dark blue) and DD neutron source (orange). Solid blue (red) lines indicate the median of the ER (NR) simulated distributions, and the dotted lines indicate the 10% and 90% quantiles. Thin gray lines show contours of constant electron-equivalent energy (keV_{ee}) and nuclear recoil energy (keV_{nr}). This shows the distinction of NRs to ERs in LZ. Figure from [8]. 22

9 The HV electrode configuration for the LZ TPC, shown next to a photograph of the fully assembled TPC. The lighter purple indicates GXe and darker purple LXe. Figure from [10]. The extraction region labelled in the diagram is the electroluminescence region; the extraction region lies at the LXe and GXe interface. 24

10 Overview visualisation of the Xe purification system. Figure from [11]. 26

11 Image of an acoustic sensor unit (left) comprising of two acoustic sensors as well as the installation location of three of the acoustic sensors units on the LZ ICV (right). Eight acoustic sensors in total are installed on the ICV, six at 120° intervals around the ICV, following the positioning of A and B around the ICV as well as one on the top (C) and one on the bottom. 30

12 'Left - waveform taken during dripping tests. Right - waveform taken during bubbling tests. There is a clear difference between the two. The waveform from the drip has a lower frequency and a secondary structure associated with the rebound of the liquid surface. The waveform from the bubble has a fast, higher frequency response but is of lower amplitude.' - from LZ's Preliminary Design Review. 30
13 Image of a loop antenna installed on one of the PMT trusses. 32
14 Left: Sparking signal type pulse. Middle: Bipolar spike type noise. Right: Periodic interference, from [12]. 33
15 Simulation Event Display with interference and adaptive trigger, from [12]. 33
16 Image of a WPS (left) and the geometry of the capacitors (right). . . . 35
17 "(Top): Voltage increases as the beaker is being filled." "(Bottom): The periodic change is caused by the impact of oil droplets on the liquid surface" - from [13]. 36
18 Liquid level measurement influenced by the TPC pressure but not applied field - from [13]. 37
19 Flowchart of the software developed. The multiple arrows from the "Batch Processing" box indicate parallel processing, a new one core job is created for each run to be processed into RQs up-to a set limit. Once this limit has been reached, jobs will wait until another is done before being ran. 39
20 Plots showing the acoustic sensors (AS), loop antenna (LA) and weir precision sensors (WPS) average ADC counts over $\approx$ 8 days. Average ADC counts being the average value for an event, averaged over all sensors for each sensor type. Red vertical lines are placed at 0651MT highlighting the periodic activity seen in the LA & AS. Green vertical lines are placed when the 6022SV and 6012SV solenoid valves are actuating, which is also seen in the LA & AS. The large deviation from WPS baseline on the 2024/01/29 is from a change of cryocoolers, representing a $\approx$ 0.5mm level change. 43

21 Moving averages, window size of 0.5ms, centered about 0 for each sensor, of different events, along with the PMT waveforms for the event. Different colours represent the individual input channels for each sensor; acoustic sensors are on the left hand side of the page and loop antenna on the right hand side. 44
22 Plot highlighting the time period when the 8118SV was manually actuated in green. The manual actuation matches well with the signal seen in the daily actuations. No signal is seen at 0651MT on 06-05 due to LED calibrations. Whilst the AS signal amplitude does not look similar to the other valve actuations in this graph, it should be noted that this amplitude varies, Figure 20 shows evidence of this with a longer time peroid of data displayed. 45
23 Average ADC Count of the individual WPS' over a period of a week. This reveals that signals are coming from mainly just two of the sensors. 47
24 WPS Locations around the LXe surface in the TPC - WPS3 and WPS5 are situated next to eachother. 48
25 Three different types of event waveforms seen by the WPS sensors. It is consistent for all the signals, including for events where only WPS3 or WPS5 have a signal (which are not shown above), that the "signal" comes from a single bin significantly different in value from the rest. . . 49
26 Histogram showing the time difference between peaks in events where 2 peaks are observed (either in the same WPS, or different WPS); a negative time difference for WPS3 $\rightarrow$ WPS5 indicates the first peak was in WPS5. Given the discreteness of this data it is likely, although not confirmed, that the cause of the signals are from the same source and the time difference between the peaks account for the different distances between the weir sensors and source. 50

27 Liquid level heights from peaks in the events from December 1st to December 20th 2023; the peaks were found using a simple peak finder algorithm, checking whether a sample was higher or lower than both its neighbours to be classified as a peak, the 5 highest peaks for each sensor, per event were saved. Due to most events containing only noise, most of these peaks are from noise fluctuations and give us an understanding of the liquid level baseline as well as the surface height of the highest peaks (and troughs). It is clear that many peaks in WPS3 and WPS5 are not physical due to the calculated level height observed being significantly larger than the height of the sensor. 51

28 Plot of average ADC count for each fast sensor over December 2023. Periods of hotspots are highlighted in green. There is no clear correlation between any signal in the sensors and periods when hotspots are present. 53

29 Plot of average ADC count for each fast sensor over around the end of May 2024. A 3.7 magnitude Earthquake is highlighted in green; this is not seen by the fast sensors. 55

30 Plot of average ADC count for each fast sensor over August 2023. Times when PMTs are tripped are highlighted in blue. There is no clear correlation between any signal in the sensors and times when PMTs are tripped. The large spikes seen in the WPS are from a power outage and a change of circulation compressors respectively. 57

31 Plot of average ADC count for each fast sensor over November 2023. Times when PMTs are tripped are highlighted in blue. There is no clear correlation between any signal in the sensors and times when PMTs are tripped. The large gap in the data is from a power-outage at the SURF site, it is noted the liquid level height was different after the outage compared to before; this level change is less than 0.1mm and is due to insufficient control over the liquid level. 58

1 Dark Matter

The Standard Model of Particle Physics encompasses our best knowledge and understanding of Physics and, although it has stood the test of time, we know that it is not complete.

Throughout history there has been interest in what we cannot see to explain observations which don't fit our current models' predictions, an example being the luminiferous aether to explain how light could traverse a vacuum whilst being a wave and the Michelson Morely experiment to test this postulate [14]. Although our current models are near-perfect at predicting everything that we can see; much like history, our interest has shifted to what we cannot see to explain the imperfections - objects known as being 'dark' - as solutions to phenomena that the model does not predict.

Astrophysical observations indicate that the mass-energy of the Universe is comprised of only $\approx 4\%$ normal matter, which the standard model explains. The remaining mass-energy is split into 26% Dark Matter and 70% Dark Energy which are not explained by the Standard Model [15, 16].

The evidence for Dark Matter is overwhelming and observed across all scales of the Universe. This chapter outlines evidence for Dark Matter as well as potential particle candidates.

1.1 Evidence for Dark Matter

1.1.1 Velocity Dispersion

Evidence for Dark Matter started mounting as early as the 1930s when unexpected orbital dynamics were observed in the Coma Cluster by Zwicky. The virial theorem:

$$\langle V \rangle = -2\langle K \rangle \tag{1}$$

where $\langle V \rangle$ and $\langle K \rangle$ are the time averaged potential and kinetic energy of the cluster respectively; was used to infer the mass of the cluster from the velocity dispersion. This was compared to luminosity observations and a mass to luminosity ratio of the cluster was calculated to be around 500:1. This is unexpectedly large when compared to 3:1 for our own galaxy. This large ratio led to Zwicky suggesting that optically invisible matter could explain the mass leading to higher orbital velocities [17].

This was not the end to observed higher-than-expected velocities in galaxies or clusters. The orbital velocity of objects as a function of distance from a galactic center, $v(r)$, according to Newtonian gravity, behaves as:

$$v(r) = \sqrt{\frac{GM(r)}{r}} \tag{2}$$

for a galaxy with mass distribution $M(r) = 4\pi \int \rho(r) r^2 dr$, and G is the gravitational constant. The majority of mass of a galaxy is concentrated within a radius R of its center. Assuming a constant density, $\rho(r) = \rho$ to approximate $M(r)$; the velocity is expected grow linearly as $v(r) \propto r$ for $r \leq R$ and decay as $v(r) \propto r^{-\frac{1}{2}}$ for $r > R$, i.e. beyond the luminous center. However, observations show that the rotation curves flattens at large distances from the luminous center rather following $v(r) \propto r^{-\frac{1}{2}}$. This indicates that the density should scale as $\rho \propto r^{-2}$ beyond the luminous center; it is this which implies the existence of a dark-halo with $\rho \propto r^{-2}$ [18]. Figure 1 shows the rotational curve for galaxy NGC 2903 with a dark-halo contribution included to explain observations; this is not a standalone observation and is observed in many galaxies [19].

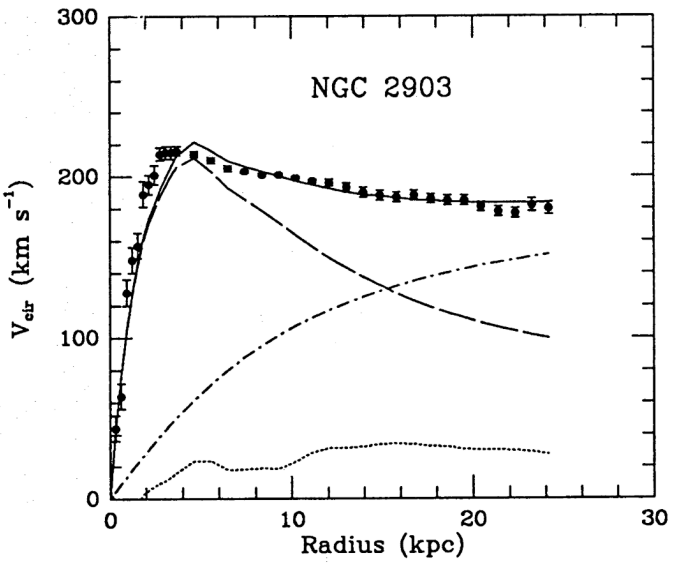


Figure 1: Rotational curve of galaxy NGC 2903 with a dark-halo fit. The dashed line shows the visible matter contribution; the dotted line shows the gas contribution and; the dot dashed line shows the contribution from the Dark Matter halo. Figure taken from [1].

1.1.2 Weak Gravitational Lensing & The Bullet Cluster

Weak gravitational lensing, predicted by General Relativity, can be used to infer the gravitational potential of a galaxy by observing how it curves the light from more distant background objects behind the galaxy. This effect is similar to light curved from an optical lens but the focal length is instead dependent on the mass content of the galaxy [20]. This effect has been used to map the mass distribution of many galaxies, one of the most notable being the Bullet Cluster.

The Bullet Cluster is often hailed as the "smoking gun" as direct empirical proof of the existence of Dark Matter. Luminous (non-dark) matter and Dark Matter components of galaxies, given sufficient time, acquire similar centrally-symmetric distributions with a common gravitational potential [21]. During collisions of galaxies, the inter-cluster plasma, the dominant luminous mass component of galaxies, experiences ram pressure whilst the rest of the luminous matter behaves almost as collisionless particles; thus, the plasma and the rest of the luminous matter spatially decouple. The location of the plasma can be mapped as it is X-ray emitting. Given the plasma is the dominant luminous mass component, the gravitational potential should follow a similar form.

However, in the presence of Dark Matter this potential would be shifted towards the location of the non-dominant luminous matter, given the Dark Matter could also be modelled as collisionless.

Weak gravitational lensing was used to map the gravitational potential of the Bullet Cluster and X-rays were used to map the location of the plasma in the Bullet Cluster; Figure 2 shows the results of the mappings. The gravitational potential does not coincide with the X-ray emitting plasma but is more consistent with the presence of a dominant population of collisonless Dark Matter [21].

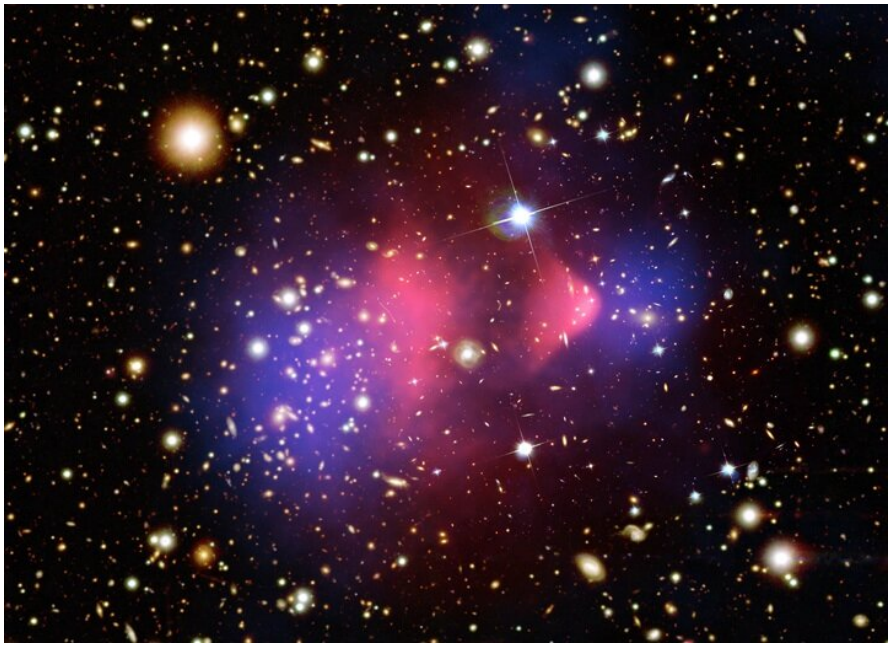


Figure 2: False colour image of the bullet cluster. Pink shows the region of hot gas, containing most of the visible matter the clusters. Blue shows the regions where most the mass is found using weak gravitational lensing. Image credit: X-ray: NASA/CXC/M.Markevitch et al. Optical: NASA/STScI; Magellan/U.Arizona/D.Clowe et al. Lensing Map: NASA/STScI; ESO WFI; Magellan/U.Arizona/D.Clowe et al.

1.1.3 The Cosmic Microwave Background

The Cosmic Microwave Background (CMB) provides some of the most important observations and tests of cosmological theory. The CMB is a relic of the early Universe when it was roughly 380,000 years old and is seen in all directions at a temperature

of around $2.7K$ [22]. Whilst mostly uniform, the CMB exhibits small fluctuations in temperature of order $10^{-5}K$ which provide a wealth of information.

The origins of the CMB come from the epoch of recombination; as the Universe expanded and cooled, neutral hydrogen atoms were able to form, emitting photons as the electrons dropped to the ground states. The change from a hot plasma to neutral atoms meant the Universe went from opaque to transparent meaning those photons emitted were the first to be able to travel the Universe (with a mean free path equal to approximately to the size of that), this phenomenon is known as photon decoupling. These photons, red-shifted since $z \approx 1100$, are what we see today as the CMB.

The temperature fluctuations can be seen as oscillations in the angular power spectrum of the CMB as shown in Figure 3. These fluctuations arose from cosmological perturbations exciting sound waves in the relativistic baryon-photon fluid of the early Universe, known as baryon acoustic oscillations (BAO). Cosmological theory predicts that acoustic oscillations in the plasma will be imprinted onto the power spectrum of the CMB [23]. The angular power spectrum of the CMB fluctuations allows measurement of the cosmological parameters; the location of the first peak indicates the flat geometry of the Universe and the total energy density; the locations and heights of the second and third peaks tell us about the baryon density in the early Universe, thus also about the Dark Matter density.

The Planck Collaboration's 2018 combined analysis of measurements of the cosmological parameters measured the Dark Matter density $\Omega_c h^2 = 0.120 \pm 0.001$, and the baryon density $\Omega_b h^2 = 0.0224 \pm 0.0001$. This corresponds to an approximately 26% Dark Matter and 4% matter Universe [24].

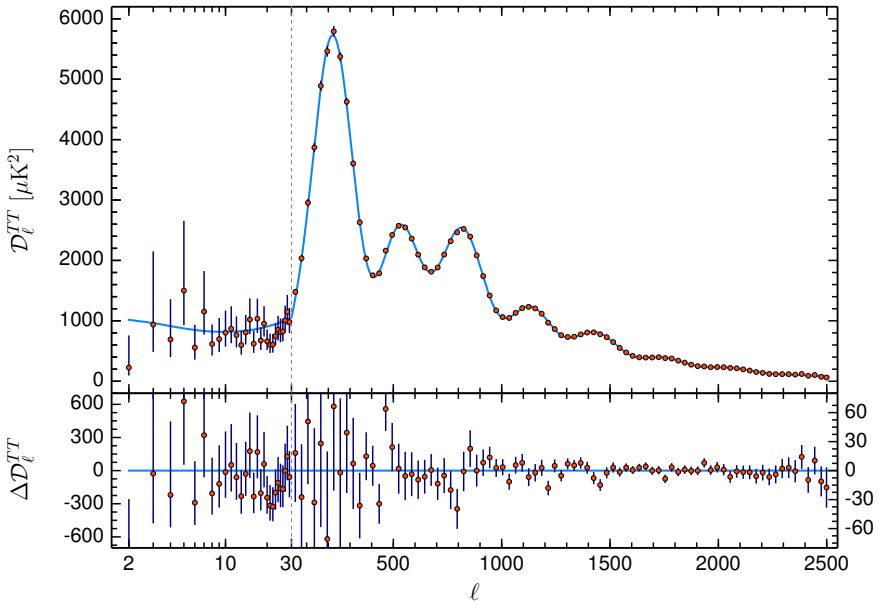


Figure 3: Angular power spectrum of the CMB, measured by the Planck collaboration, 2018. Figure taken from [2].

1.1.4 The ΛCDM Model

The Lambda Cold Dark Matter (ΛCDM) model is often referred to as the Standard Model of Cosmology. The model describes the CMB power spectrum observed, BAO, large scale structure in galaxy distribution and the accelerating expansion of the Universe. The model sets constraints on Dark Matter, namely it must be:

- Dark - that is it doesn't produce any observable signals meaning that is must be dissapationless by not cooling by radiating photons, nor interact electromagnetically or chromodynamically;
- Cold (non-relativistic) - such that large scale structures, such as halos around galaxies can be formed;
- Collisionless - Dark Matter halos have not been observed to interact with itself or baryonic matter, implying a very low cross-section for either interaction;
- Long lived - this is due to it's abundance in the early Universe persisting to the current day [25].

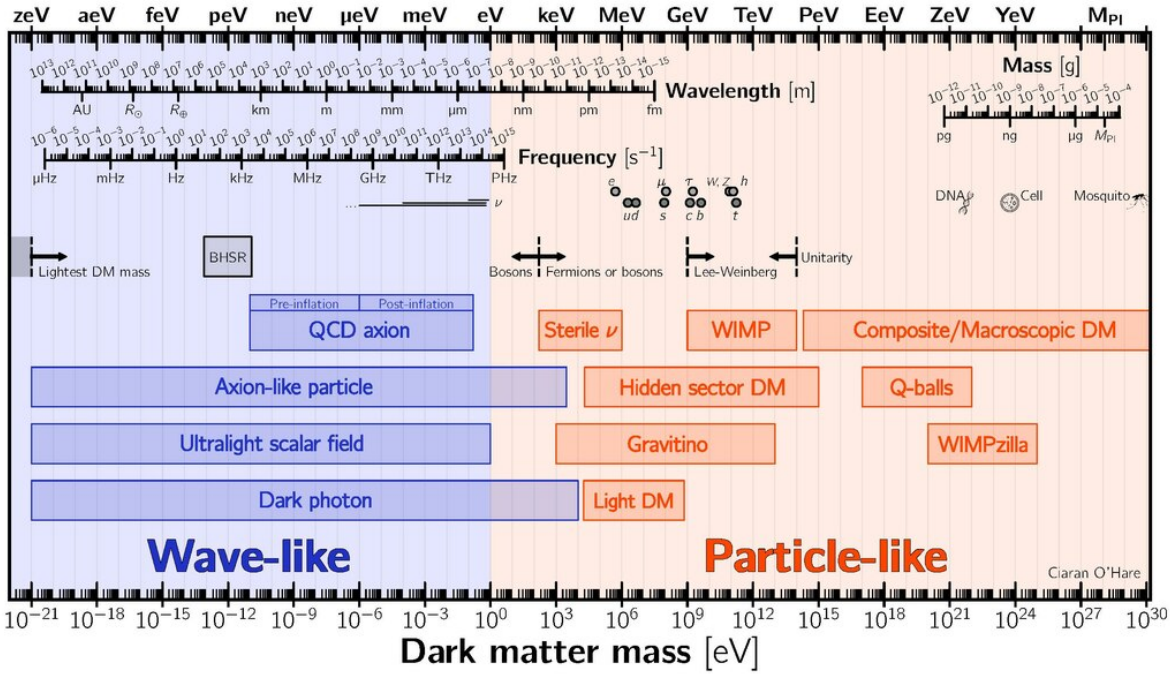


Figure 4: Overview of hypothesised Dark Matter candidates over 51 orders of mass range; split into wave-like and particle-like candidates. Figure taken from [3].

1.2 Dark Matter Candidates

The evidence for Dark Matter is overwhelming, as is the number of theorised candidates. As outlined in the previous section, the ΛCDM model outlines essential constraints on Dark Matter candidates. Figure 4 visualises the most popular candidates over 51 orders of mass range. This chapter briefly summarises a couple of these Dark Matter candidates.

1.2.1 WIMPs

WIMPs, Weakly Interacting Massive Particles, are a collection of possible candidates for Dark Matter. These candidates interact with gravity and the weak force, are massive, cold, and stable relics from the early Universe from freeze-out. WIMPs are created thermally: in the early Universe, when it was a high temperature, thermal equilibrium was obtained where the number density of each particle species was roughly equal to the number density of photons. As the Universe expanded and cooled below the WIMPs mass, creation of WIMPs became rare and shortly after the WIMP density dropped

to a point where annihilation of WIMPs also became rare, leading to a freeze-out in the number density. Remarkably, for the relic density to be equal to that observed in cosmological measurements, the interaction strength is that expected on the order of the electro-weak scale [26].

WIMPs could also provide a solution to the gauge hierarchy problem in Particle Physics [27]. The hierarchy problem is the question why the Higgs Boson's mass is so small; a possible solution could involve an extension to the standard model, allowing new particles to cancel terms to quantum corrections on the Higgs mass - this is solved by super symmetry where neutralinos pose a viable WIMP Dark Matter candidate [28]. Due to the expected interaction strength being that of the electro-weak scale and simultaneously providing a solution to the gauge hierarchy problem, WIMPs are a popular Dark Matter candidate and conned the "WIMP miracle".

1.2.2 Neutrinos

Standard model neutrinos were an early popular candidate for Dark Matter, a large part of this was their "undisputed virture of being known to exist" [29]. There are, however, flaws with standard model neutrinos as Dark Matter candidates, namely: they are not abundant enough to make up a dominant component of Dark Matter and; they are relativistic collisionless particles which isn't favoured by the ΛCDM model.

Sterile neutrinos, however, could be a possible Dark Matter candidate. Sterile neutrinos are hypothesised right-handed neutrinos which resolve the issue of the neutrinos experimentally determined mass, which the standard model doesn't predict. Sterile neutrinos would allow neutrinos to acquire mass through the same mechanism as that of quarks and charged leptons. Depending on their mass, sterile neutrinos could be a suitable candidate for Dark Matter [28, 18].

1.2.3 Axions

Axions were introduced as an attempt to solve the strong CP problem. Pecci and Quinn showed that introducing a $U(1)$ symmetry which was spontaneously broken could explain the strong CP problem. The spontaneous symmetry breaking implied the existence of the Goldstone boson, also known as the Axion [30]. Axions with a

mass range between 10^{-6} to 10^{-4} eV are a popular Dark Matter candidate. Although their small hypothesised mass, Axions are thought to have an extremely weak coupling such that they were never in thermal equilibrium, therefore could exist as a cold dark matter [31].

2 The LUX-ZEPLIN Experiment

2.1 Overview

The LUX-ZEPLIN (LZ) experiment is a generation-2 (G2) direct Dark Matter detector consisting of 7 tonnes of active liquid Xenon (LXe) in a dual-phase (liquid-gas) time projection chamber (TPC) with a primary goal of setting world-leading sensitives to WIMP nucleon interactions, or, detecting WIMPs.

2.1.1 2022 Sensitivity Result

LZ set world-leading limits for spin-independent WIMP-nucleon interactions above $10\text{GeV}/c^2$ with its first science run (SR1) results released in 2022 [8]. Figure 5 shows the sensitivity plot released by the LZ collaboration in 2022, showing world leading sensitivities at a 90% confidence level for spin-independent WIMP-nucleon interactions.

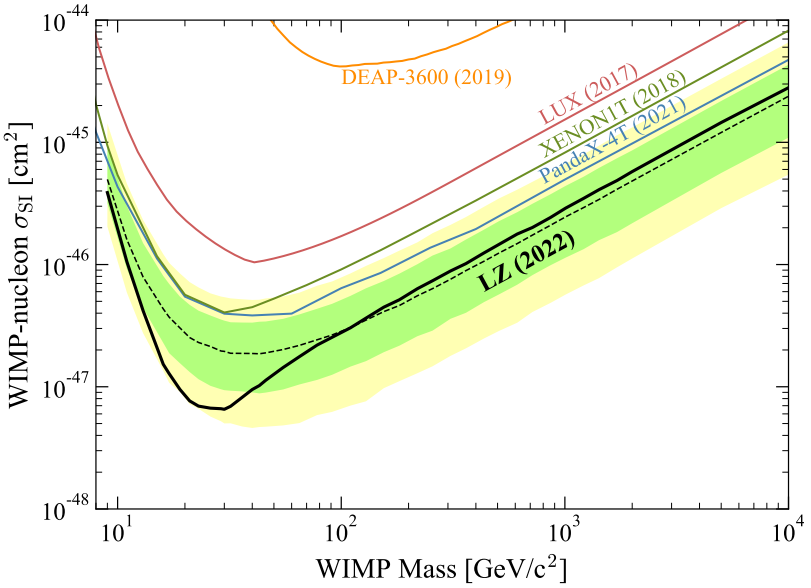


Figure 5: LUX-ZEPLIN's 2022 sensitivity result with 60-live days of data taking; published in 2023. The 90% confidence limit for the spin independent WIMP cross section vs. WIMP mass is shown by the black line. The green and yellow bands are the 1σ and 2σ sensitivity bands respectively. The dotted line shows the median of the sensitivity projection. Limits are also shown from the PandaX-4T [4], XenonNT [5], LUX [6] and DEAP-3600 [7] experiments. Plot from the LUX-ZEPLIN SR1 results paper [8].

2.1.2 Detector Overview

LZ's dual-phase LXe TPC is housed within a field cage which is within the inner cryostat vessel (ICV) [11]. Inside the cavity between the field cage and ICV is a LXe "skin" with 131 PMTs used for vetoing backgrounds. The ICV is inside a Gadolinium Liquid Scintilator (GdLS) outer detector, which itself is within a 228 tonne water tank with 120 PMTs, both again for background discrimination and vetoing capabilities [32]. See Figure 6 for a visualisation of the LZ detector. Within the TPC are HV grids used to create a vertical electric field to drift electrons towards the gaseous extraction region of the TPC and produce electroluminescence.

This chapter provides an overview of the LZ detector with detail in the named parts above.

2.2 The Time Projection Chamber

The heart of LZ is it's dual-phase TPC. Figure 7 outlines the operating principle of the dual phase TPC in LZ for particle detection. Particle interactions in the liquid Xenon (LXe) cause excitation and ionisation of the Xenon. The excited Xenon dimer, Xe_2*, quickly decays emitting scintillation photons which are detected by the PMTs as prompt scintillation, this is known as the S1 signal.

$$\mathrm{X} + \mathrm{Xe} \longrightarrow \mathrm{Xe}^* + \mathrm{X} \qquad \text{Recoil and Excitation} \qquad (3)$$

$$\mathrm{Xe}^* + \mathrm{Xe} \longrightarrow \mathrm{Xe}_2^{*,v} \qquad \text{Excimer Formation} \qquad (4)$$

$$\mathrm{Xe}_2^{*,v} \longrightarrow \mathrm{Xe}_2^* + \mathrm{X} \qquad \text{Relaxation} \qquad (5)$$

$$\mathrm{Xe}_2^* \longrightarrow \mathrm{Xe} + \mathrm{Xe} + \gamma \qquad \text{Photon Emission (S1)} \qquad (6)$$

The electrons from the ionisation are drifted towards the gaseous region of the TPC; using a vertical electric field - see section 2.2.1; where they generate electroluminescence, creating a second signal seen by the PMTs, this is known as the S2 signal.

These signals can be used to distinguish electronic recoils (ERs) from nuclear recoils (NRs) as they differ in their ratio of ionisation electrons and scintillation photons (S2/S1); this can be seen as two separate bands when plotting $\log_{10}$(S1/S2) against

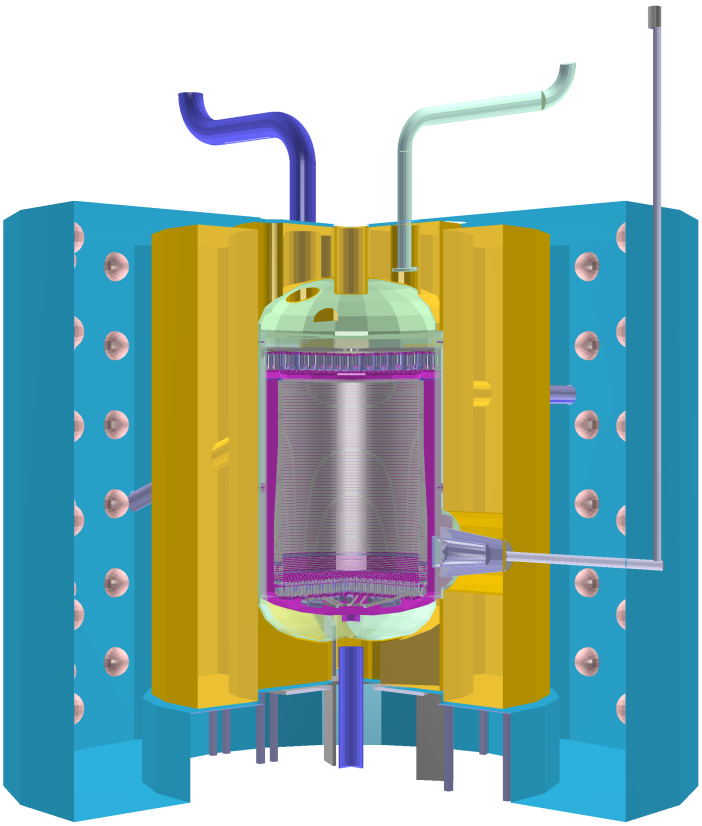


Figure 6: Visualization of the LZ detector in BACCARAT (Basically, A Component-Centric. Analog Response to AnyThing - an LZ simulation package built on GEANT4). The TPC (magenta) within the cryostat (light green) is surrounded by the GdLS outer detector tanks (yellow) that are immersed in a water tank. The inner part of the water tank within the PMT structure is shown in blue. Figure and caption taken from [9].

S1 as shown in calibration data for SR1 in Figure 8.

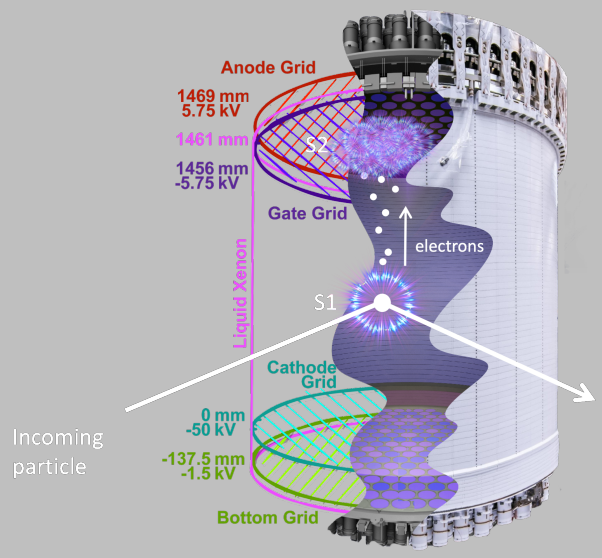


Figure 7: Operating principle of the dual phase Xe TPC. Particle interactions in the liquid Xenon (LXe) produce two energy signatures; scintillation photons (S1) and electrons which are drifted by a vertical electric field into the gaseous phase of the Xe and are observed as electroluminescence (S2). The LXe surface lies between the anode grid and gate grids as shown by the pink outline with the gaseous phase lying above. The PMTs are located above and below the anode grid and bottom grid respectively. Note: The shown applied voltages are varied between science runs to meet the needs of the experiment.

Xenon is a popular choice in liquid noble detectors due to a few reasons, predominantly [33]:

- Xenons relatively high atomic mass, $M_{Xe} \approx 120$ GeV/c^2, provides a good kinetic match to WIMP masses of order 100 GeV/c^2; this is the WIMP mass scale predicted by freeze-out;
- Its high atomic number, $Z = 54$, and density, $\approx 3g/cm^3$, means it has the highest stopping power out of the rare noble gases;
  - Due to Xenons high stopping power and the size of the LZ detector, which is larger than the mean interaction length of neutrons and gamma rays, as well as the TPCs ability to 3D reconstruct the position of interactions, the LXe is self-shielding. This allows for a fiducial volume to be defined inside

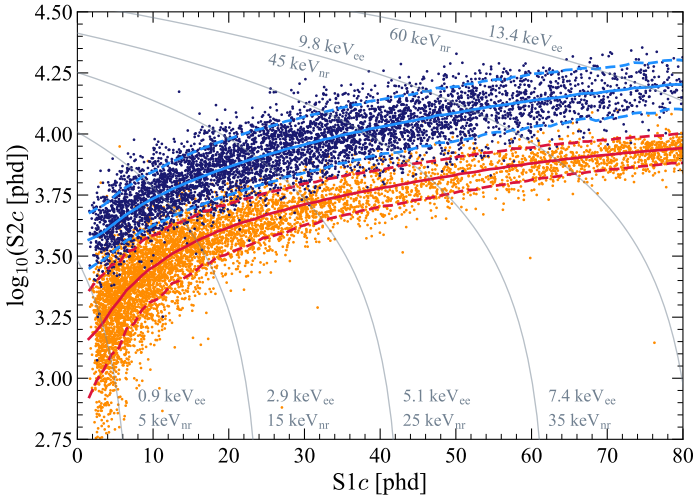


Figure 8: Calibration events used in SR1 plotted as $\log_{10}$S2c-S1c for the tritum source (dark blue) and DD neutron source (orange). Solid blue (red) lines indicate the median of the ER (NR) simulated distributions, and the dotted lines indicate the 10% and 90% quantiles. Thin gray lines show contours of constant electron-equivalent energy (keV$_{ee}$) and nuclear recoil energy (keV$_{nr}$). This shows the distinction of NRs to ERs in LZ. Figure from [8].

the TPC which is shielded by external backgrounds by a layer of LXe.

- Xenon possess the ability to create a scintillation and ionisation response to particle interaction, which is only shared with liquid Argon (LAr) among the liquid rare gases;
  - Xenon also has the highest ionisation and scintillation yields between itself and Argon, whilst also having a fast response time.
- A large majority of naturally radioactive isotopes of Xenon have a half-life less than a month, simplifying the purification process for contaminants.

Argon is also used at competing Dark Matter experiments, primarily due to its greater availability and lower price. This enables detectors of much larger masses to be created, such as DarkSide-20k which plans for a 20 tonne LAr detector [34]. Argon pays for the ability to host detectors of larger mass with the trade-off of lower scintillation and light yields as well as the fact that LAr contains Argon-39, a long lived radio-isotope which contributes an additional background. Argon can be sourced from underground which does not contain this isotope, but care is required when bringing it to the surface as

cosmogenic activation can create Argon-39 isotopes [35], making Ar more difficult to maintain radiopurity than Xenon.

2.2.1 High-Voltage Grids

The electrostatic environment of the LZ TPC is defined by four woven mesh grids [10]. The grid set-up is illustrated in Figure 9 and consists of, from top to bottom of the TPC: an electroluminesence region, an extraction region, a drift region and a reverse field region; created by an anode, gate, cathode and bottom woven wire mesh grids.

These grids establish a vertical electric field within the TPC, the drift region, to drift electrons from interactions in the LXe to the extraction region where the interface of the LXe and GXe lies. Electrons experience a much greater electric field in the electroluminescence region in order to increase the electron extraction probability and produce S2 signals. The bottom grid is used to establish the reverse field region which is important for protection of the bottom PMTs from the electric field; electrons produced from interactions in this region are not extracted and only an S1 signal is seen from these interactions.

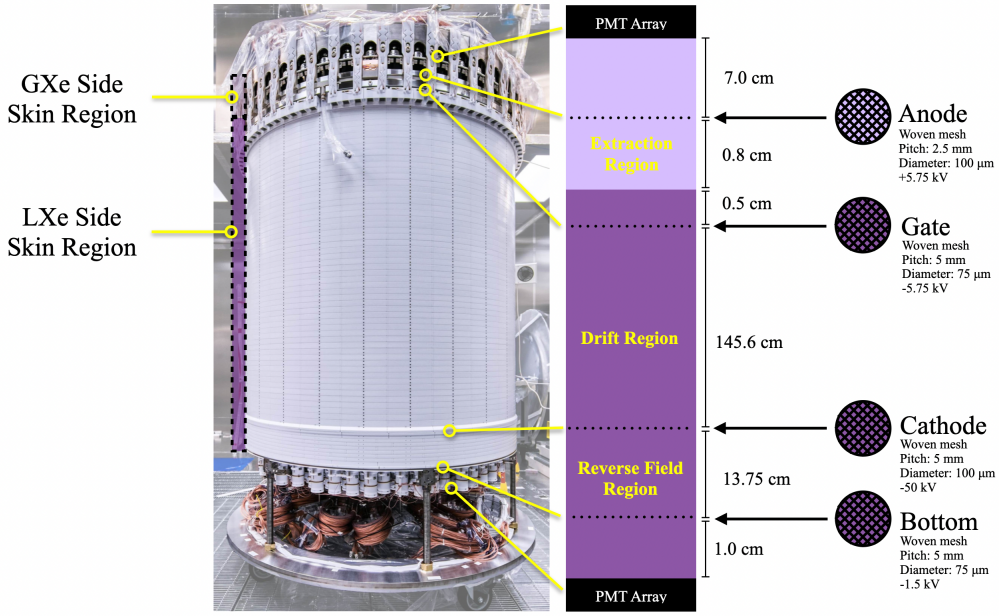


Figure 9: The HV electrode configuration for the LZ TPC, shown next to a photograph of the fully assembled TPC. The lighter purple indicates GXe and darker purple LXe. Figure from [10]. The extraction region labelled in the diagram is the electroluminescence region; the extraction region lies at the LXe and GXe interface.

2.3 The Veto Detectors & Water Tank

The Veto Detectors, also known as the Outer Detector System (ODS), is split into two main sections; the Skin and the Outer Detector.

Neutron radiation can scatter elastically and fake a WIMP signal within the TPC. However, unlike WIMPs, neutrons are also likely to interact again within the TPC or nearby, therefore, the ODS is desirable in-order-to fill as much of the neighbouring volume as possible with radiation detectors to search for these multiple scatters [32]. Additionally, the Veto Detectors will be able to veto external interactions where VUV photons could leak into the TPC, faking an S1 signal.

The Skin consists of between 4cm to 8cm of LXe between the field cage and cryostat; an even thicker region, known as the dome skin, exists below the bottom PMT array [32]. There are 131 PMTs observing the skin region; split into 93 1-inch PMTs and 20 2-inch PMTs in the side of the Skin and 18 2-inch PMTs in the dome region.

The Outer Detector is a near-hermetic gamma-ray and neutron anti-coincidence system. The detector is formed from acrylic tanks filled with gadolinium doped liquid scintillator which are observed by 120 PMTs within the water tank. The gadolinium has a high neutron cross-section, enhancing the scintillator's neutron capture capabilities.

The Veto Detectors also introduce more material that has gone through a stringent radio-assay campaign between the TPC and cave walls, attenuating backgrounds observed from the cave walls.

The LZ detector is hosted within the David Campus water tank at SURF; the David Campus water tank contains 70,000 gallons of purified water which provides additional shielding from external backgrounds, particularly neutrons and gammas.

Additionally, the water tank and the ODS can detect and veto Cherenkov radiation from cosmic muons.

2.4 Xenon Circulation and Purification

The Xenon within LZ is constantly being circulated and purified. Purification is necessary due to the large quantity of polytetrafluoroethylene (PTFE) and plastics used within the detector which serve as a source of outgassing, contaminating the Xenon. Figure 10 depicts a simple visualisation of the purification process.

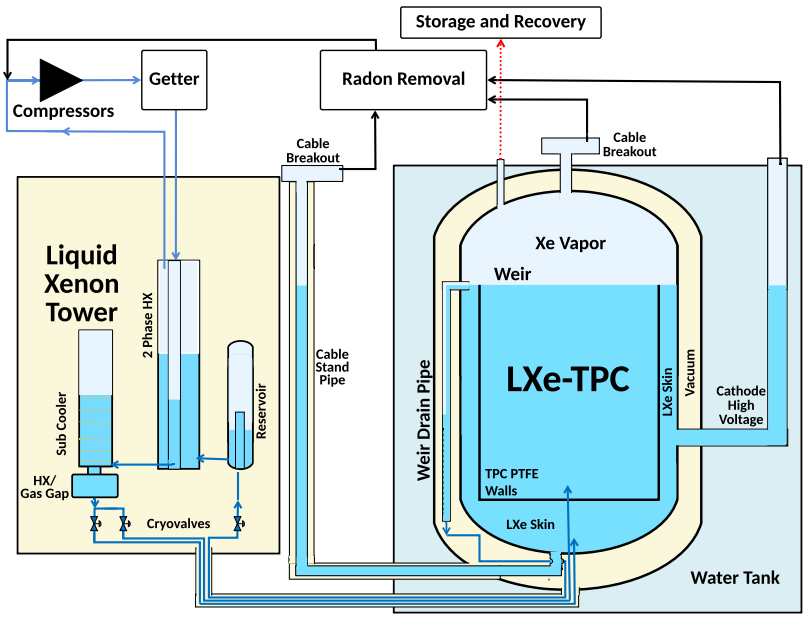


Figure 10: Overview visualisation of the Xe purification system. Figure from [11].

There are weirs installed within the TPC to control the surface level of the Xenon, Xenon over-spilling the weirs is collected in the Xenon tower. The Xenon is then circulated to a purification tank which is outside of the water tank, there is it is evaporated then passed to and purified by a commercial heated getter. After this, it is returned to the liquid tower, re-condensed, degassed, sub-cooled and then passed back into the detector [32].

In order to control the flow rate and timing for various gases and liquids required for cooling, purification and flow of the Xenon, various valves are used throughout LZ; including solenoid valves. These valves use electromagnetic fields to control the flow of the gases and liquids which could have a measurable effect on the electromagnetic environment within the detector.

2.5 Internal Monitoring Sensors

LZ hosts numerous sensors, including: thermometers, long level sensors, loop antenna, acoustic sensors, pressure transducers and, weir precision sensors. Data acquisition for the sensors can be split broadly into two categories, slow control and fast control. Data acquired via slow control is sampled continuously at 1Hz and is used by operators of the detector to monitor for long-term changes and make any adjustments as required to meet the needs of the experiment.

Data acquired by fast control is triggered on PMT events, in a 2.5ms window centered on the S2 of events, at a 100kHz sampling rate. Only the acoustic sensors (AS), loop antenna (LA) and, weir precision sensors (WPS); dubbed the "fast sensors"; are included in this data acquisition. The fast control sensors are of particular interest because their data has been rarely analysed since the experiment's commissioning, as other analyses have taken priority. In contrast, slow control data is well understood, having been consistently used to monitor long-term detector changes. Additionally, Oxford contributed the detector monitoring system, including the development and testing of: acoustic sensors, loop antennae and, weir precision sensors within the detector; therefore it follows that Oxford analyses this data.

LZ uses a software package called LZ Analysis Package (LZAP); LZAP takes in raw data of PMT pulses and generates reduced quantities (RQs) for physics analysis. RQs are derived physics quantities that condense the waveform of each PMT pulse into a handful of key parameters, summarising the waveform's characteristics for efficient processing and analysis on a large scale.

Although fast control sensor data is recorded into the same files that LZAP takes as input, it is not included in LZAP analysis, thus is not accessible for quick analysis. The aim of this project is to develop a framework to create RQs of, as well as analyse data from the fast sensors to explore and understand whether any un-explained anomalous behaviour in the PMTs can be linked to the detector environment seen by the fast sensors. Through this, this will also fulfil an additional goal to make the fast data from the sensors more accessible to the collaboration for future use.

LZ hosts 8 acoustic sensors (AS), 8 loop antenna (LA) and, 6 weir precision sensors

(WPS). The materials chosen for the sensors need to include consideration of trace radioactive elements due to the sensitivity requirements of the experiment, whilst additionally operating safely at cryogenic temperatures. The materials initially underwent screening in Germanium Detectors at the Boulby Underground Laboratory and showed acceptable cleanliness [12]. Post-assembly, the sensors were screened at SURF before being installed into LZ.

2.5.1 Acoustic Sensors

The AS consist of a piezoelectric PVDF dielectric and two silver electrodes which collect the charge [32]. They are designed to detect spurious vibrations which could contribute towards backgrounds and an unwanted internal environment for the TPC, such as the cavitation of bubbles. The sensor readout is differential, therefore, each sensor unit consists of a pair of sensors, see Figure 11, where the voltage gradient between the sensors, $V = \frac{\Delta V}{\Delta x}$, is digitised and recorded. The sensors were designed with the concern of motion in the $\hat{r}$ direction of the TPC to be able to detect vibrations traveling in the $\hat{\phi}$ (cylindrical co-ordinates) direction around the ICV. There is very low sensitivity to vibrations traveling in the $\hat{z}$ direction around the ICV due to the differential readout of the sensors spaced in the $\hat{\phi}$ direction.

The AS were tested at low temperatures using liquid nitrogen. Bubble detection was observed and calibrated using water-based set-up (water is a similar acoustic impedance to Xe) where air was injected into the water to create bubbles - see Figure 12 for the results of this test. The sensors were also installed in the SLAC System Test - a large LZ system test plarform containing more than 100 kg of LXe to demonstrate their bubble detection capabilities.

Given the 100kHz sampling rate of fast control and the 4mm spacing of the strips, this enables a discrimination of vibrations up to $v \simeq 4000 ms^{-1}$ in the $\hat{\phi}$ direction around the ICV.

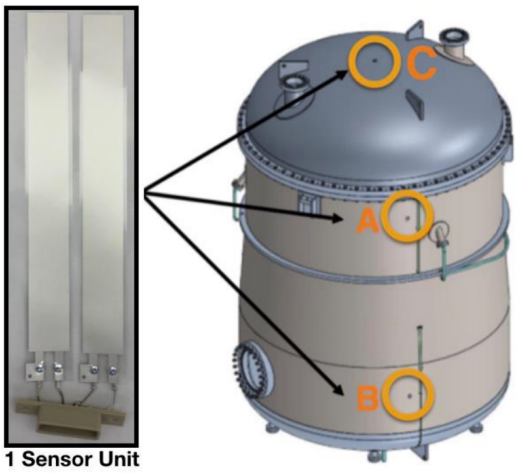


Figure 11: Image of an acoustic sensor unit (left) comprising of two acoustic sensors as well as the installation location of three of the acoustic sensors units on the LZ ICV (right). Eight acoustic sensors in total are installed on the ICV, six at 120° intervals around the ICV, following the positioning of A and B around the ICV as well as one on the top (C) and one on the bottom.

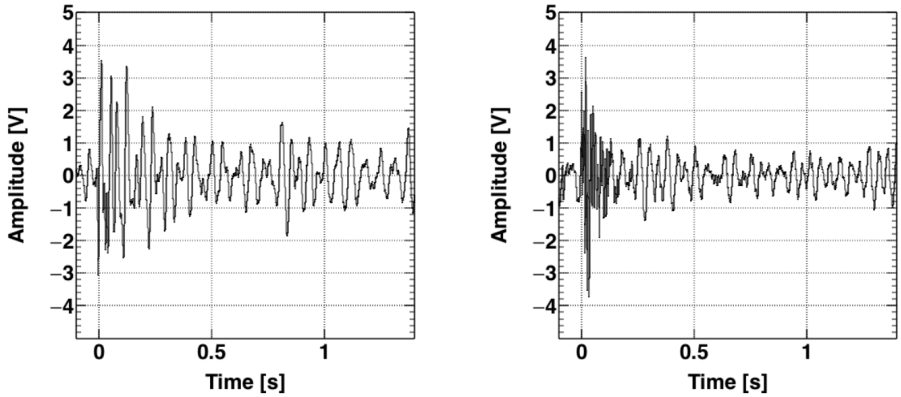


Figure 12: 'Left - waveform taken during dripping tests. Right - waveform taken during bubbling tests. There is a clear difference between the two. The waveform from the drip has a lower frequency and a secondary structure associated with the rebound of the liquid surface. The waveform from the bubble has a fast, higher frequency response but is of lower amplitude.' - from LZ's Preliminary Design Review.

2.5.2 Loop Antenna

The aim of the LA is to detect EM waves emitted by a possible high-voltage (HV) discharge from the grids, particularly during a pre-breakdown discharge period and especially during the break-down period. An adaptive trigger was implemented during LZ's commissioning to quickly identify sparks and notify slow control users such that the high voltage grids could be reduced before the detectors internals are damaged - particularly the PMTs [32].

A derivation, found in [12] (p150), reduces the discharges to a current flowing over a spark gap, which is modeled as a RLC circuit with the arc developing a self-inductance L_α and resistance R_α. This gives the discharge a power-spectrum defined by:

$$P_{arc}(t) = \frac{k^2 \dot{I}_{arc}(0)^2 \omega^2}{(\omega_a^2 - \omega^2) + (4\alpha^2\omega^2)} \tag{7}$$

where $\alpha = \frac{R_\alpha}{2L_\alpha}$, $\omega = \frac{1}{\sqrt{L_\alpha C_s}}$, C_s is the capacitance through an inductor and resistor connected in series and, k and ω_a are constants.

This shows that the discharges have a well defined EM signature which can be used for their detection. Additionally, the LA serve as a way to identify for periods of electric field instability within the TPC which could contribute spurious backgrounds [12].

The LA are made of 2 stacked OFHC copper wire rings using 2mm diameter wire in a 35mm radius loop, held in place by a polyether ether ketone casing (PEEK) [12]. There are four loop antenna installed evenly spaced on the top PMT truss and four on the bottom PMT truss. See Figure 13 for an image of a LA.

The Loop Antenna's response to radiation from a discharge was initially tested by creating a spark in air and measuring the LA's response; the spark was created by an ignition coil. The LA underwent further testing at the SLAC System Test with 2 LA installed above and below the TPC during the test. The electric fields reached in the SLAC Systems Test were of the same order of magnitude expected to that of LZ, therefore making an ideal test environment for the LA. High voltage ramp tests and spark discharge tests were performed; the results of this showed similarity to the spark tests performed in air and are shown in Figure 14. This additionally showed that

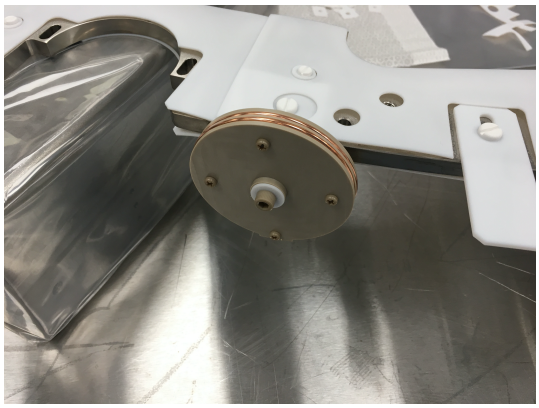


Figure 13: Image of a loop antenna installed on one of the PMT trusses.

the LA were sensitive to the EM environment in a setup similar to LZ. An adaptive trigger to notify slow control users of sparking was created from the data gathered in the Systems Test as well as simulations of sparking events, Figure 15 shows a simulated time period and the adaptive trigger threshold. Post-installation in the LZ detector, a functionality test was conducted by creating a spark with a piezo-electric crystal and recording the response of the LA - all LA passed this test [12].

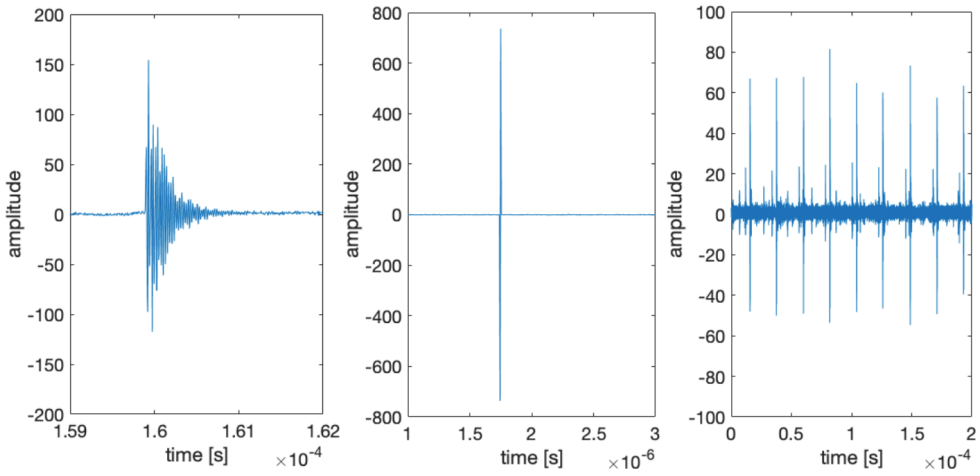


Figure 14: Left: Sparking signal type pulse. Middle: Bipolar spike type noise. Right: Periodic interference, from [12].

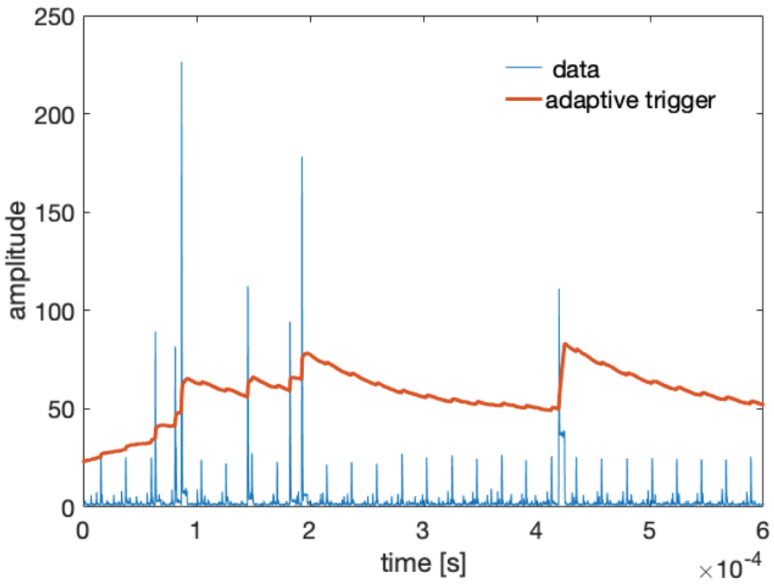


Figure 15: Simulation Event Display with interference and adaptive trigger, from [12].

2.5.3 Weir Precision Sensors

The WPS are parallel plate capacitors made out of OFHC copper with the liquid surface lying between the plates, they have a precision of $\approx 10\mu m$ [32]. The WPS are used to measure the surface height of the LXe, including the capability for the detection of ripples and waves. See Figure 16 for an illustration of the WPS geometry and build. The voltage readout for a parallel plate capacitor with two different dielectrics lying in a parallel configuration between the plates can be written as:

$$R = \frac{V_{adc}}{V_E} = \frac{C_{ref} - C_{lvl}}{C_{ref} + C_{lvl}}, \tag{8}$$

where $V_{adc} = 4096$ is the ADC count, V_E is the excitation voltage of the op-amp in the sensor, C_{ref} is a reference capacitor within the sensor and, C_{lvl} is the liquid level measurement capacitance given by:

$$C_{lvl} = (C_{LXe}^{-1} + C_{GXe}^{-1})^{-1}, \tag{9}$$

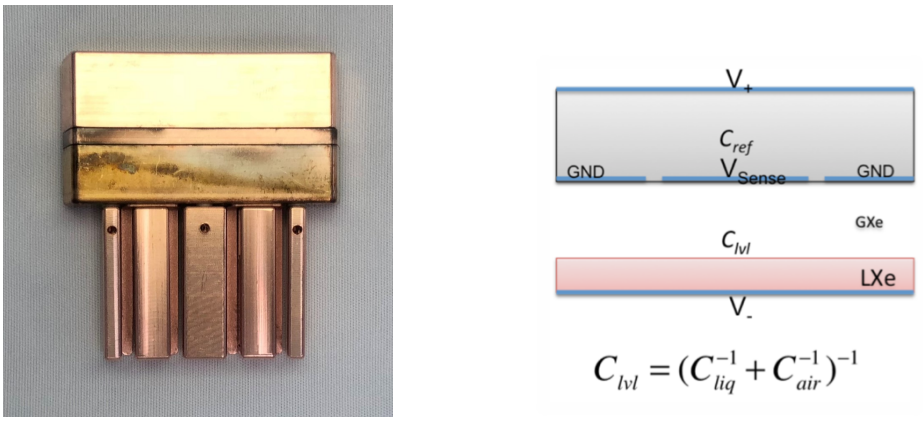
This can be converted into a liquid level height , $z(R,T)$, which is given by:

$$z(R,T) = \left(\frac{L}{\epsilon_{LXe}(T)}\right) \cdot \left(\frac{1+R}{1-R} \cdot \frac{C_{ref}(T)}{C_{lvl}(T, z=0)} - 1\right), \tag{10}$$

where T is the temperature of the sensor or liquid, L is the measurement range of the sensor, ϵ_{LXe} is the dielectric constant of the liquid Xenon [13].

There are six WPS installed evenly spaced around the LXe surface in the TPC along with an additional one installed within the TPC for calibrating the others during the filling stages of the TPC with LXe.

In order to test the response of the WPS to liquid level changes, a preliminary test where a container was filled by dropping mineral oil droplets into the container was carried out. The results of this test are shown in Figure 17 - the variations detected correspond to a $6.2 \pm 0.4\mu m$ variation in liquid level [13].



(a) Weir Precision Sensor **(b)** Geometry of the WPS

Figure 16: Image of a WPS (left) and the geometry of the capacitors (right).

Figure 18 demonstrates that the TPC pressure influences the liquid level measurement, but not the applied electric field during the SLAC Systems Test - figure from [13].

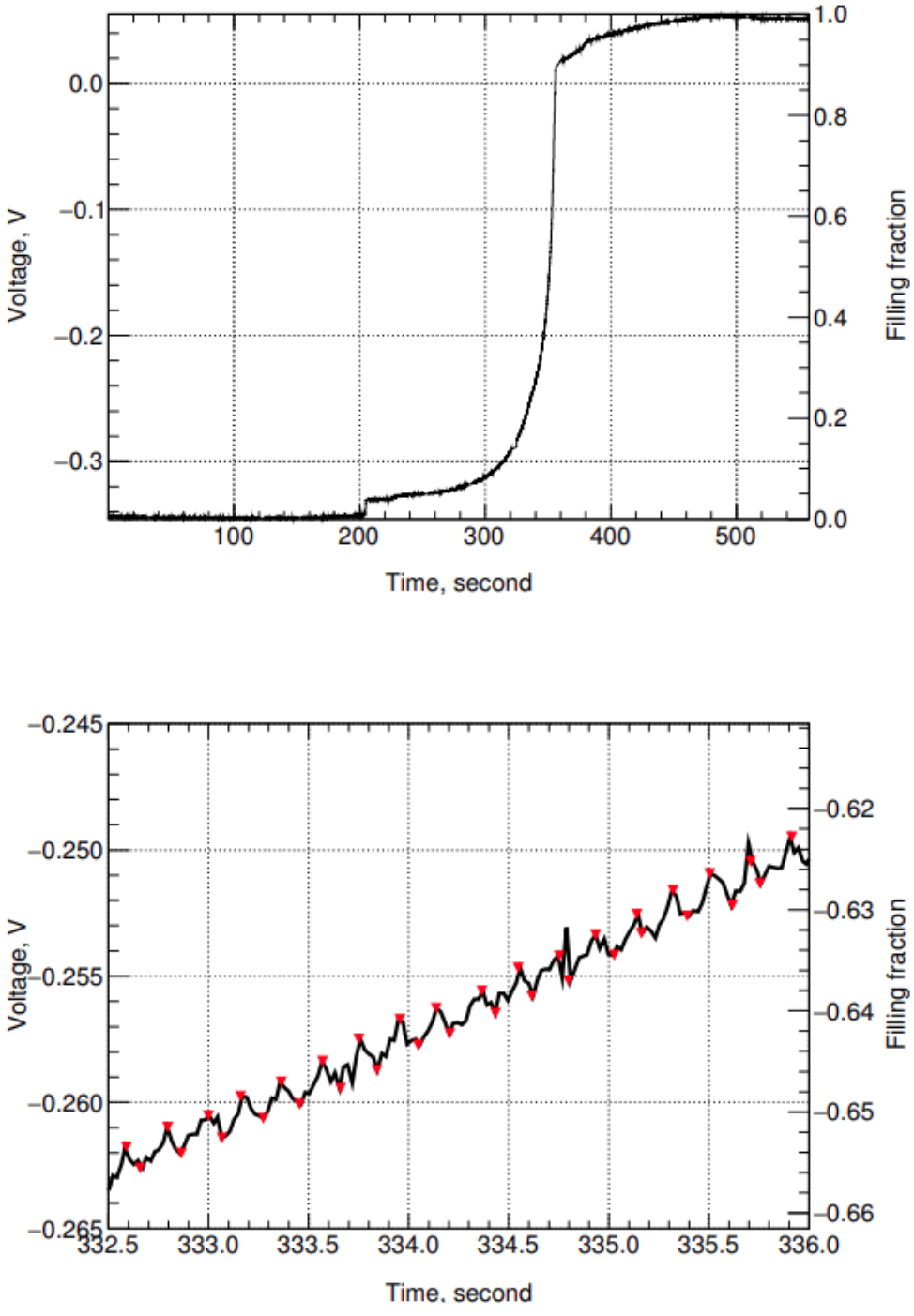


Figure 17: "(Top): Voltage increases as the beaker is being filled." "(Bottom): The periodic change is caused by the impact of oil droplets on the liquid surface" - from [13].

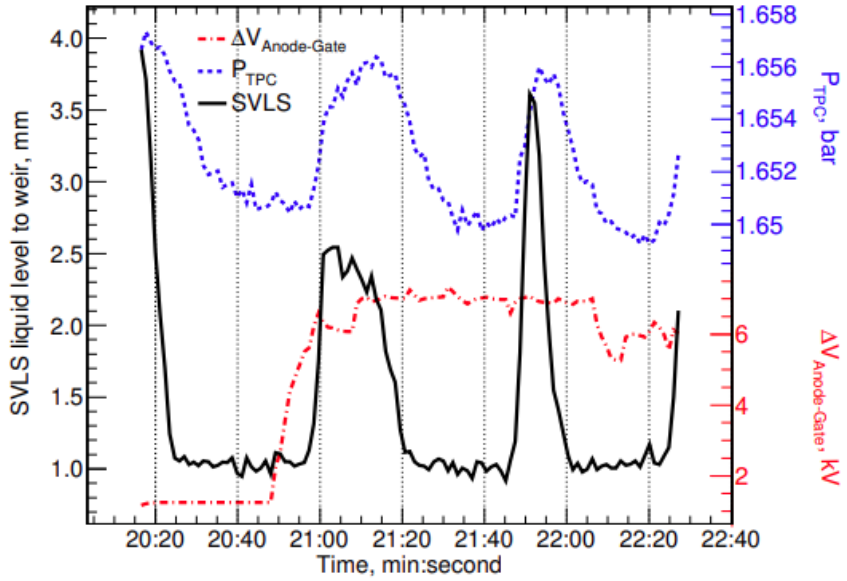


Figure 18: Liquid level measurement influenced by the TPC pressure but not applied field - from [13].

3 Fast Sensor Analysis Framework

The framework developed for analysis of the fast sensors had wide-ranging goals and was developed by myself, from scratch. The primary goal of the software was to make the fast sensor data easily accessible to the rest of the collaboration through well laid out, understandable, adaptable and modular code with desirable analysis features included. Broken down into individual goals, this included:

- Functionality to quickly hand-scan the fast sensors from an input list of events;
- Create RQs of fast control raw data from an input of either a date-range or run-range;
  - Including functionality to easily add RQs in the future;
- Analyse, and, find outlier events from RQs;
  - Including functionality to quickly make plots of RQs for investigation.
  - Calibrate the voltage read-out from the sensors to useful physical values, such as converting to liquid level height in the level sensors.

These few features together largely increased the accessibility to the fast control data, enabling studies to take place to test theories about backgrounds from the experiment which could be explained using the sensors.

In LZ, data is organised into runs, with each run typically contains around 2×10^5 events, with ≈ 3 to 10 runs conducted per day, depending on the detector's activity and run mode - modes such as calibrations increase the event rate from the decays of the calibration sources. There are 600 files per run which total to around 120GB of data/run. Due to the large amounts of data being handled which can mount into the 10s of TBs during analysis, how the data is handled w.r.t. computing limitations is at the center of the framework. Additionally, the logistics of finding and handling tens of thousands of ROOT files from the raw data required careful consideration in order to not loose any data during processing. RQs are created from the raw data which are subsequently used for the main portion of analysis - some packages were developed to look at raw data in more detail from events found in analysis of the RQs.

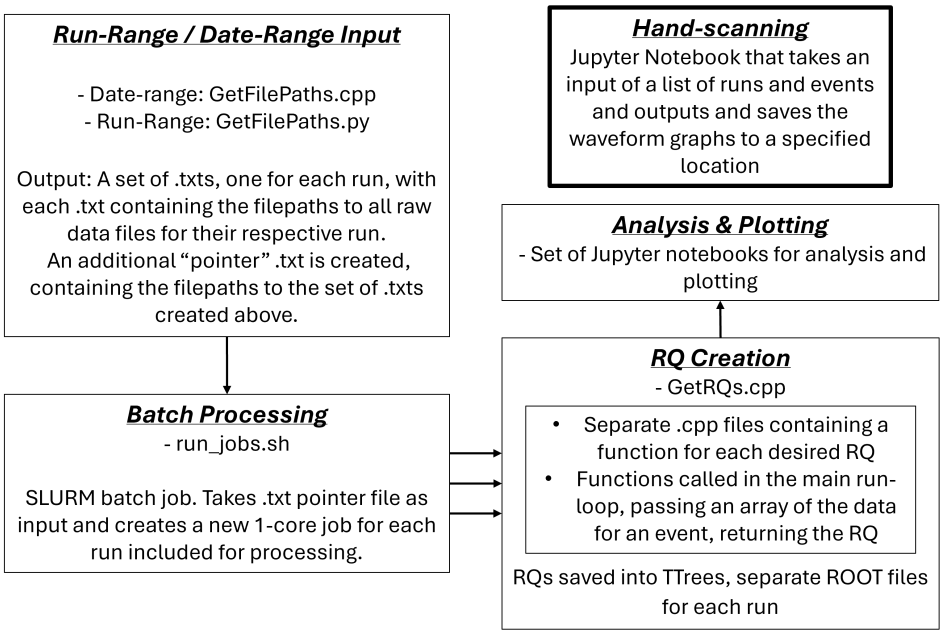


Figure 19: Flowchart of the software developed. The multiple arrows from the "Batch Processing" box indicate parallel processing, a new one core job is created for each run to be processed into RQs up-to a set limit. Once this limit has been reached, jobs will wait until another is done before being ran.

The framework used a mixture of Python, C++ and ROOT with SLURM used for batch processing; Figure 19 briefly outlines the structure of the software. C++ was chosen to generate RQs from the raw physics data because of its ease of use, particularly given ROOT's scripting interface in C++. More importantly, C++ offers improved performance compared to Python which is useful when handling such large quantities of data. Juypter notebooks and Python scripts were used for analysis post RQ creation.

The analysis uses a simple outlier detection algorithm; the average event value was 3σ outside of the mean of the average value of the run, and, is additionally seen in at least 2 of the same sensor type; i.e. 2 of the level sensors out of the 6. Whilst this can detect most short-term changes, this fails to detect longer-term changes, thus this was combined with visual analysis of time-averaged graphs showing the read-out of the sensors over a longer time-period to look for any noticeable periods of activity in the sensors.

Current RQs included of an events voltage waveform are the: mean; standard Deviation;

range; the amplitude and time of the 5 maxima/minima furthest away from the event's mean and; the 5 highest frequency peaks corresponding frequency and amplitude in the FFT spectrum of the event waveform. These are saved with meta-data including the event, run and unix time of the event.

4 Results

The analysis framework outlined above was developed and used for the results presented in this section. The section explores data from the fast sensors; particularly during periods of interest to the experiment. This includes events such as on-site power outages, to undiagnosed backgrounds in the PMTs, to identifying periods when the fast sensors produce signals and whether they can be linked to known changes in the internal environment of the detector or PMT backgrounds to help further our understanding of the LZ detector.

4.1 Solenoid Valve Actuations

The actuation of solenoid valves in the cryogenics system can be seen in both the AS and the LA. Figure 20 shows plots over time of the readout voltage, averaged over each sensor per event of the AS, LA and WPS; highlighting periods where solenoid valves are actuating. This also revealed that there was a daily event at 0651MT which was seen in both the AS and LA. Additionally, the PMT waveforms of these daily events were consistently similar and resembled e-bursts or interference. E-bursts are named backgrounds where an unusually large number of electrons are detected in the PMTs, their origins are not well understood. It was cross-checked whether the origins of all other detected e-burst events could be linked back to the actuation of the solenoid valves, it was concluded that they could not be and the solenoid valve actuation only made up a small proportion of known e-burst events.

Figure 21 shows the moving average of individual event's sensor waveforms in the AS, LA and PMTs, for typical events where: noise is observed in the sensors, a solenoid valve is actuating and, a signal observed at 0651MT. The waveforms observed in the LA for the daily 0651MT events and valve actuations are similar; the associated PMT waveforms, which show e-bursts or interference, are also similar suggesting a similar origin of these events.

It was found that the daily signal originated from another solenoid valve which actuated daily but the accepted time of the actuation was 1351MT. The error for this accepted time was presumably from a time-zone translation error as UTC (+00:00) and MT

(-07:00), the time-zone where the detector is based, have a time-difference of 7 hours; 1351UTC is 0651MT.

This was confirmed by manually operating the valve in the same manner as its daily operations, see Figure 22. It was observed that its operation can be seen in the sensors with the same signature as the daily events at 0651MT. Given that this valve automatically actuated daily but no signal was seen at 1351MT it was concluded that this was the source of the daily signals. A dive into the system operating the experiment confirmed this conclusion.

These solenoid valve actuations have been linked to time periods where elevated S1 threshold crossing rates are observed in the PMTs. That is, the light collected in the PMTs is meeting the threshold to be classified as an S1 signal at a higher rate than is typical.

The linkage between these valve actuations, increased S1 threshold crossing rates and the signal observations in the LA and AS are evidence that these sensors have fulfilled their design purpose and operation of helping understand the LZ detector's internal environment and its linkage towards backgrounds observed in the PMTs.

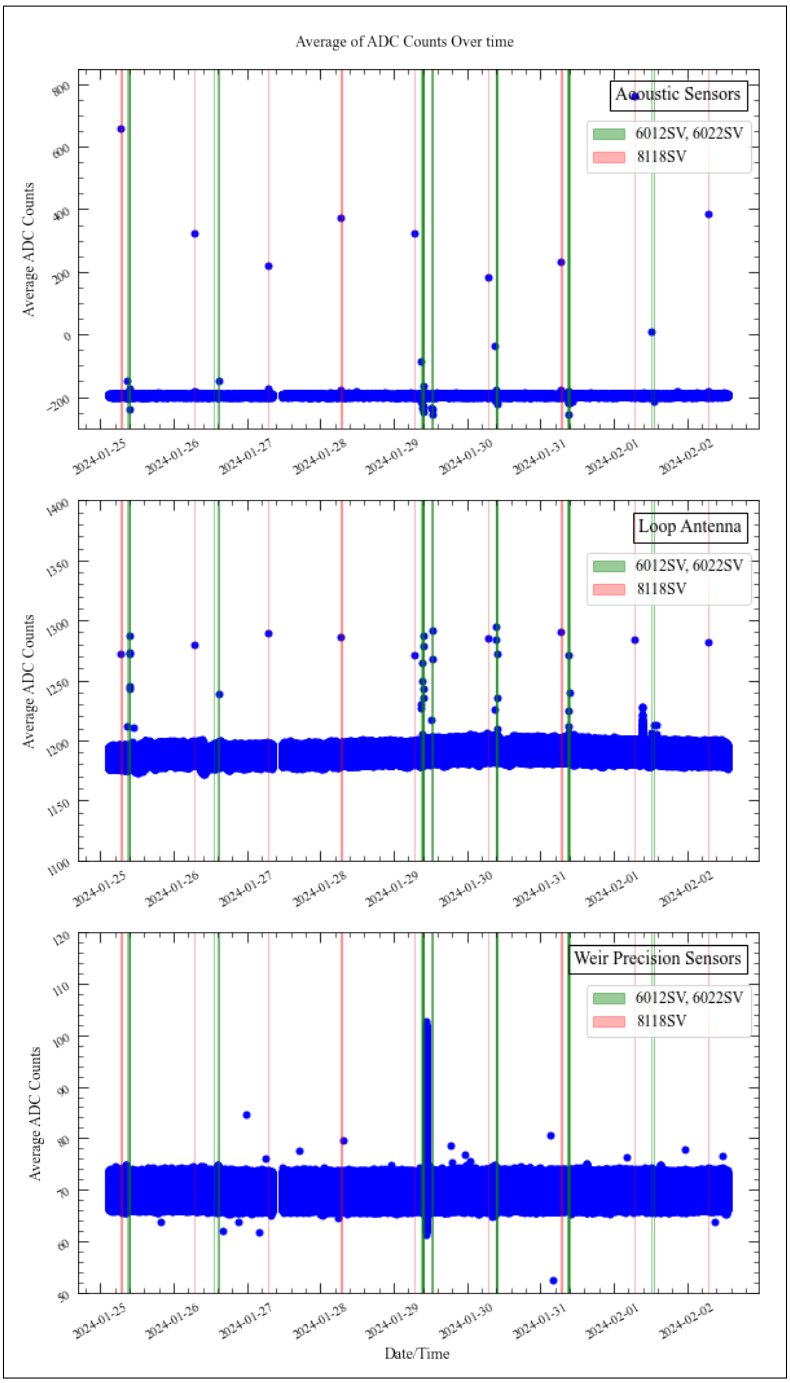
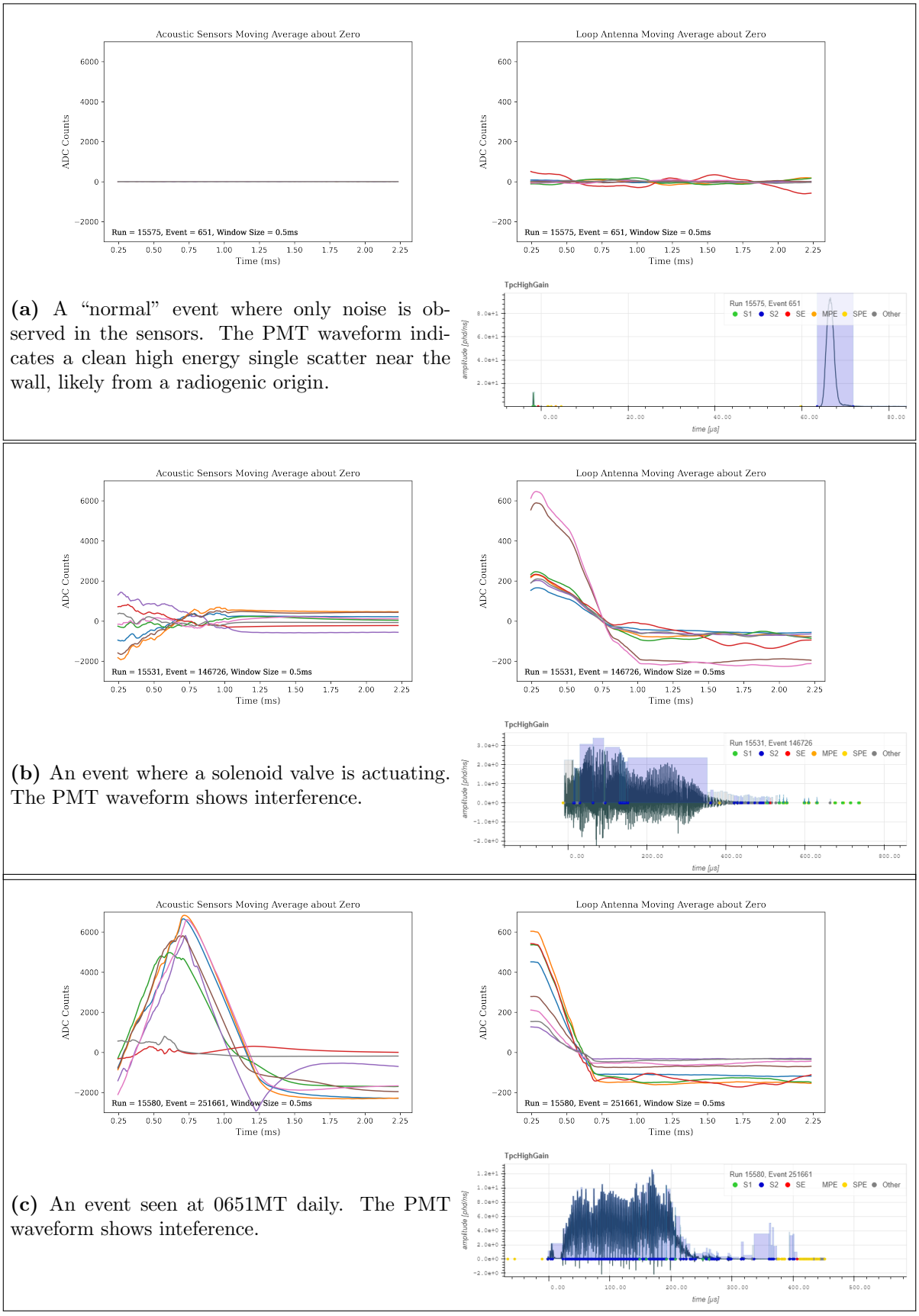


Figure 20: Plots showing the acoustic sensors (AS), loop antenna (LA) and weir precision sensors (WPS) average ADC counts over ≈ 8 days. Average ADC counts being the average value for an event, averaged over all sensors for each sensor type. Red vertical lines are placed at 0651MT highlighting the periodic activity seen in the LA & AS. Green vertical lines are placed when the 6022SV and 6012SV solenoid valves are actuating, which is also seen in the LA & AS. The large deviation from WPS baseline on the 2024/01/29 is from a change of cryocoolers, representing a ≈ 0.5mm level change.



(a) A "normal" event where only noise is observed in the sensors. The PMT waveform indicates a clean high energy single scatter near the wall, likely from a radiogenic origin.

(b) An event where a solenoid valve is actuating. The PMT waveform shows interference.

(c) An event seen at 0651MT daily. The PMT waveform shows inteference.

Figure 21: Moving averages, window size of 0.5ms, centered about 0 for each sensor, of different events, along with the PMT waveforms for the event. Different colours represent the individual input channels for each sensor; acoustic sensors are on the left hand side of the page and loop antenna on the right hand side.

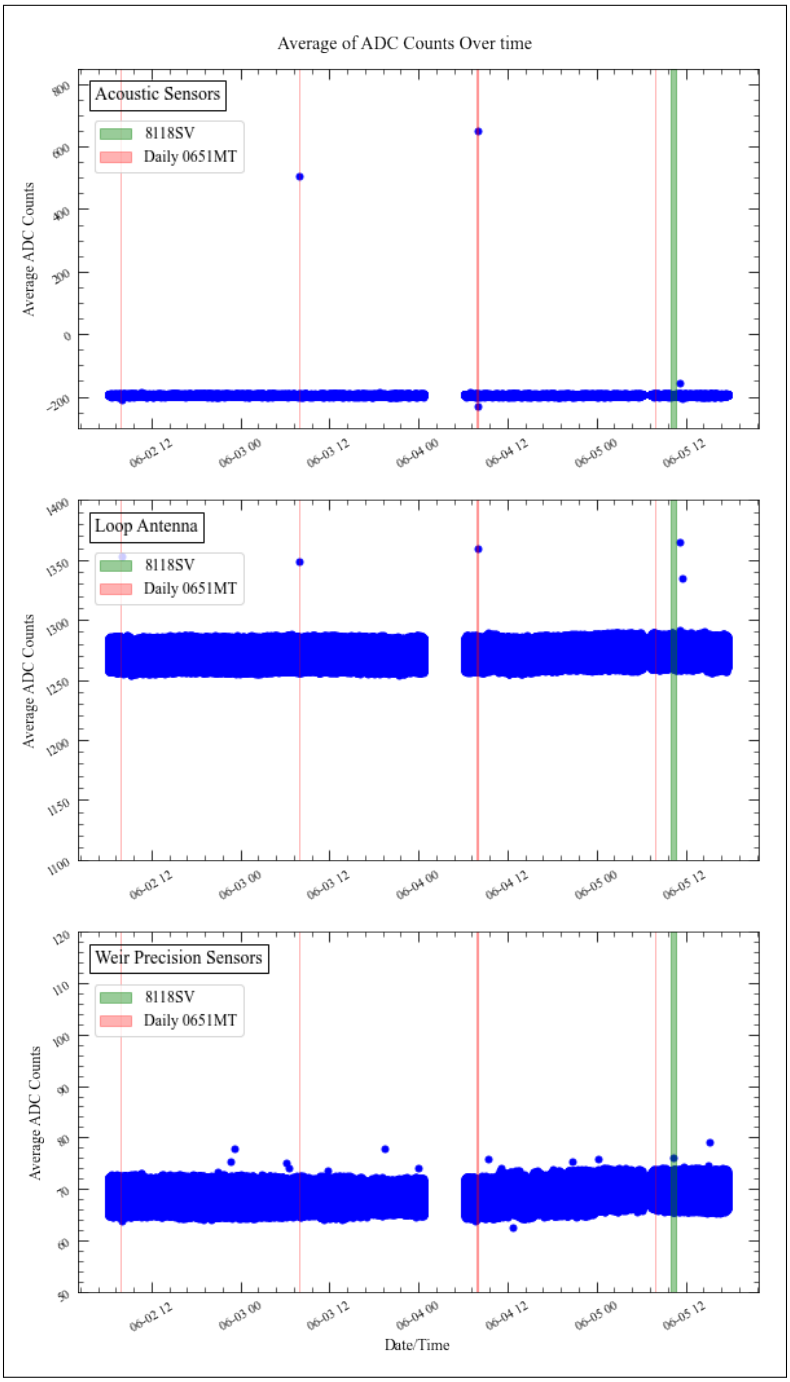


Figure 22: Plot highlighting the time period when the 8118SV was manually actuated in green. The manual actuation matches well with the signal seen in the daily actuations. No signal is seen at 0651MT on 06-05 due to LED calibrations. Whilst the AS signal amplitude does not look similar to the other valve actuations in this graph, it should be noted that this amplitude varies, Figure 20 shows evidence of this with a longer time peroid of data displayed.

4.2 Weir Precision Sensors

Whilst the signals from the AS and LA over the time period shown in Figure 20 can be explained by solenoid valve actuations, the WPS signals are not as well understood. There is a large signal seen in Figure 20 which is from a change of cryocoolers, this is also seen in slow control and already known. There are, however, many events in the fast sensors where the signals observed are not easily explained.

Figure 23 splits the WPS average from Figure 20 into individual level sensors, revealing that almost all of the signals come from just two of the sensors: WPS3 and WPS5. These two sensors are also installed next to each other - see Figure 24. It should also be noted that WPS3 and WPS5 are on the lower side of a slightly tilted LZ detector, sitting at 4.84mm lower than the WPS on the opposite sides. This results in WPS3 and WPS5 becoming a collecting point for LXe which would result in more LXe spilling into the weirs than the other side of the detector, as well as increasing the likelihood of seeing fluid motion compared to the other weir sensors.

It is also important to note that WPS3, due to installation error, or 'happy accident', was installed with an inverted polarity to the rest of the sensors. This potentially allows for cross-talk interference to be distinguished from true signals. This is because cross-talk interference would induce a signal of the same sign relative to the baseline in the sensors effected, no matter the polarity; whereas a real signal from liquid level changes would have an opposite signed signal between the sensors of opposite polarity (given the sensors both experienced a drop in liquid level, or both experienced a rise in liquid level).

Hand-scanning raw event waveforms for events where a signal is seen in the WPS, shows that every signal seen in the WPS from Figures 15,17 and 18 are from a single sample in the event being significantly higher in value compared to the rest of the data in the event. Figure 25 shows a couple of event waveforms as examples; it should be noted that there is a distinct time difference between peaks (i.e. they do not occur at the same time) and, although it is not shown in these figures, there are events where signals are only observed in one sensor.

Figure 26 shows a histogram for the time difference between the peaks of an event, for

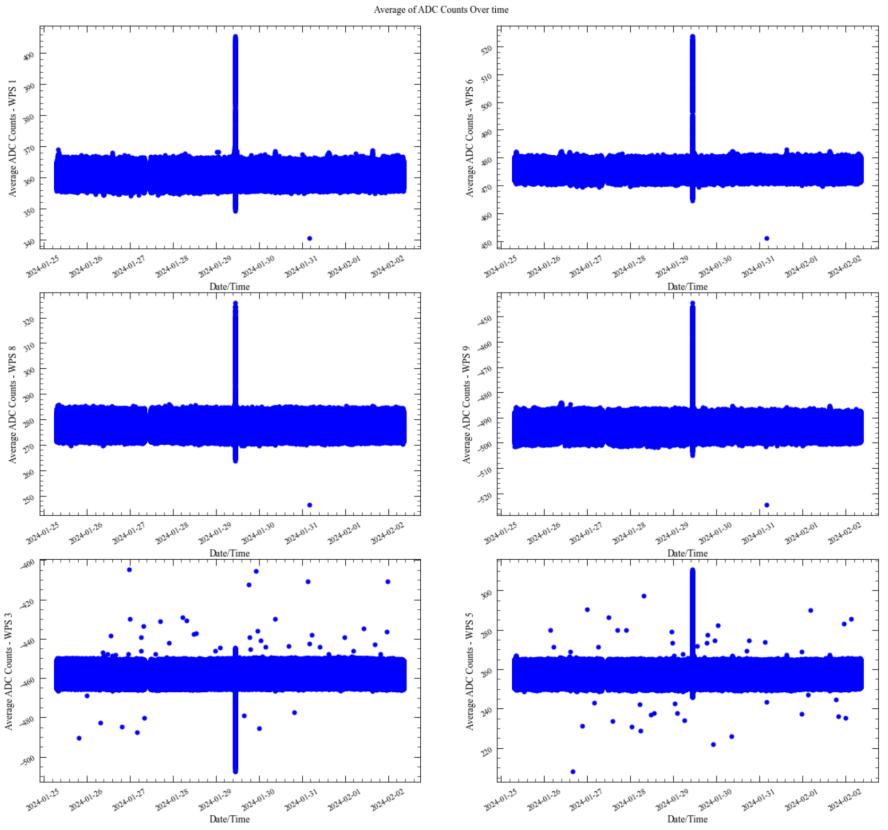


Figure 23: Average ADC Count of the individual WPS' over a period of a week. This reveals that signals are coming from mainly just two of the sensors.

when there are multiple peaks in an event, in the order that the peaks are observed. This makes an argument against the possibility of electrical interference being the root cause of the signals. Assuming an upper bound distance of $\mathcal{O}(1\text{m})$, roughly the size of the TPC, as the distance between the sensors, this would set an upper bound speed of $\approx$14km/s, or, $\mathcal{O}(10\text{km/s})$ for the time between peaks, peak, at 0.07ms. This speed is significantly lower than one would expect for electrical interference, which would be expected to travel at 50%+ of c, or $150,000\text{km/s}$. This speed is however fast enough to not be seen in the AS if the source of these signals are from vibrations.

Applying the calibrations to the WPS to calculate the liquid height from the signals must be approached with caution. The calibrations are from when the TPC was filled with LXe during the commissioning of the experiment in late 2021. Since then, there have been pressure and temperature changes inside the TPC with relative permittivity

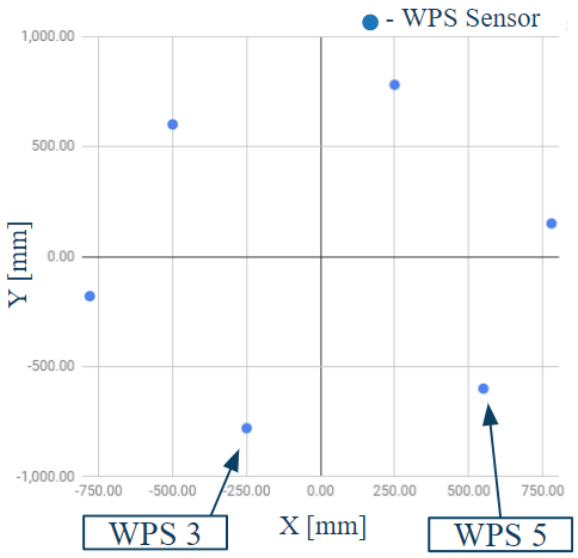


Figure 24: WPS Locations around the LXe surface in the TPC - WPS3 and WPS5 are situated next to eachother.

dependence on these changes not being well known. However, these calibrations can still be used to generate a ballpark idea of whether these signals could be physically plausible if they are from changes of liquid height, and perhaps their origin.

Figure 27 shows the liquid level heights from peaks in the events from December 1st to December 20th 2023; the peaks were found using a simple peak finder algorithm, checking whether a sample was higher or lower than both its neighbours to be classified as a peak, the 5 highest peaks for each sensor, per event were saved. Due to most events containing only noise, most of these peaks are from noise fluctuations and give us an understanding of the liquid level baseline. Given the WPS are less than 10cm in height, many of the apparent peaks in level height are not physically possible for WPS3 and WPS5. Combined with Figure 25, where the peaks are only observed for one sample, or a 10μs bin, before returning to the baseline height, provides further evidence against the signals coming from liquid level changes. Although it can be concluded that these signals are not from level changes of the Xenon surface, the source of these signals is still not well understood and more work is required to determine the source of the signals.

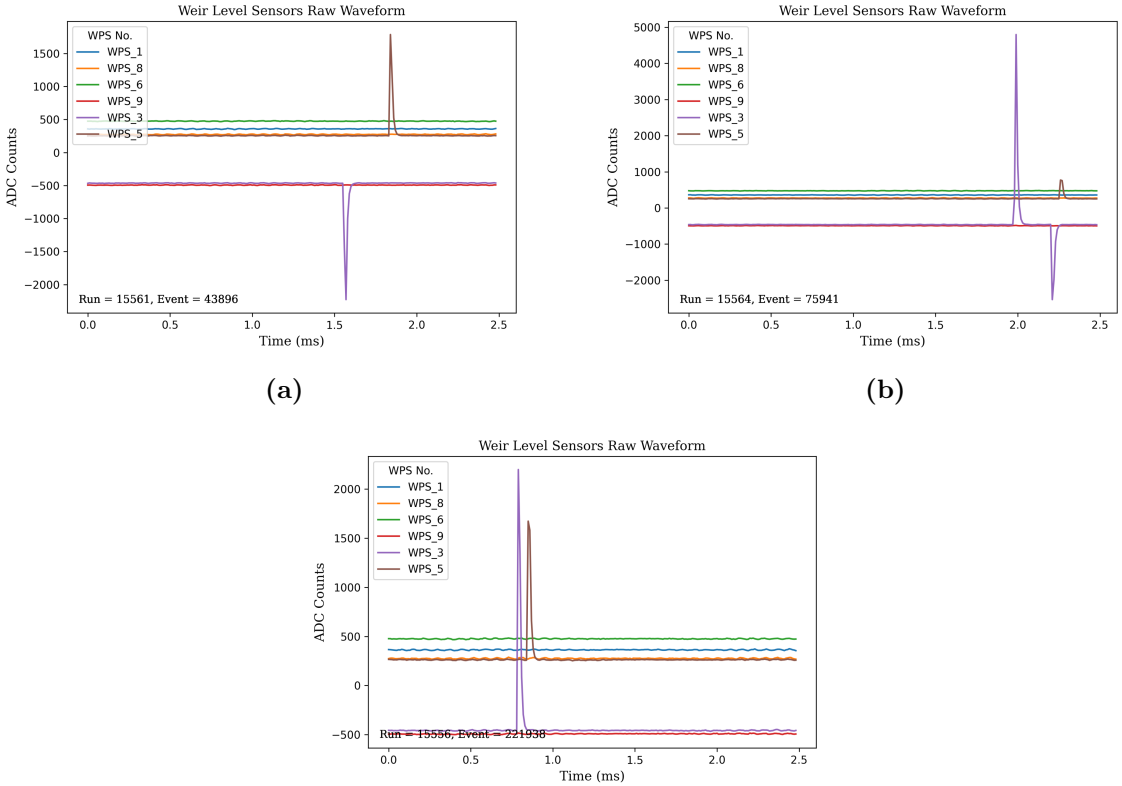


Figure 25: Three different types of event waveforms seen by the WPS sensors. It is consistent for all the signals, including for events where only WPS3 or WPS5 have a signal (which are not shown above), that the "signal" comes from a single bin significantly different in value from the rest.

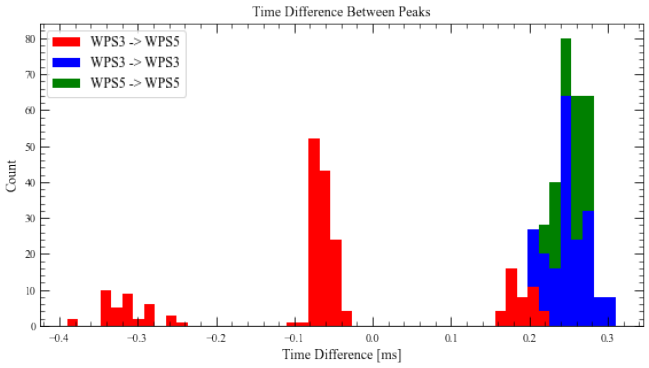


Figure 26: Histogram showing the time difference between peaks in events where 2 peaks are observed (either in the same WPS, or different WPS); a negative time difference for WPS3 → WPS5 indicates the first peak was in WPS5. Given the discreteness of this data it is likely, although not confirmed, that the cause of the signals are from the same source and the time difference between the peaks account for the different distances between the weir sensors and source.

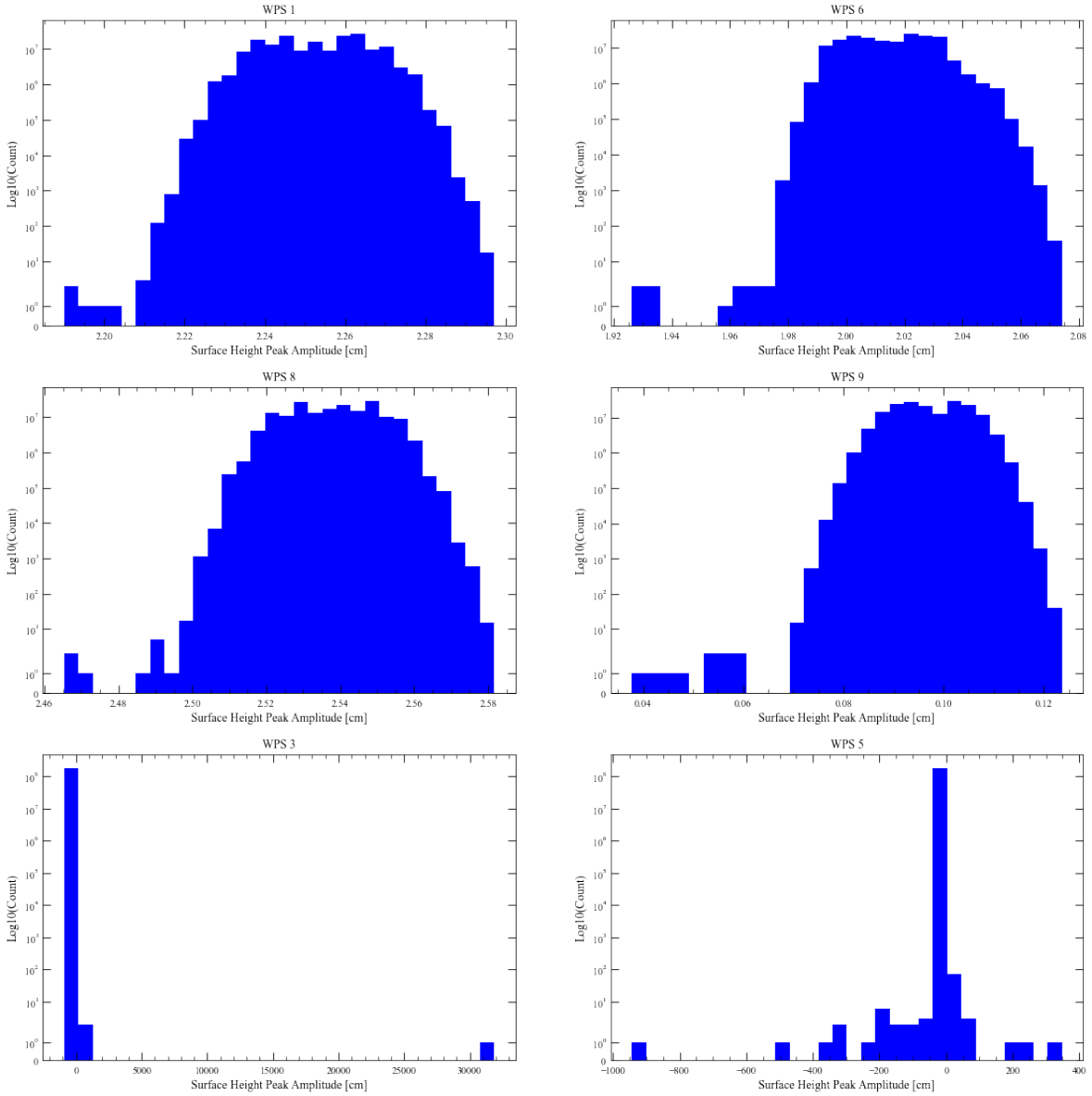


Figure 27: Liquid level heights from peaks in the events from December 1st to December 20th 2023; the peaks were found using a simple peak finder algorithm, checking whether a sample was higher or lower than both its neighbours to be classified as a peak, the 5 highest peaks for each sensor, per event were saved. Due to most events containing only noise, most of these peaks are from noise fluctuations and give us an understanding of the liquid level baseline as well as the surface height of the highest peaks (and troughs). It is clear that many peaks in WPS3 and WPS5 are not physical due to the calculated level height observed being significantly larger than the height of the sensor.

4.3 Hotspots

Hotspots are an accidental background in LZ seen as isolated S2s, that is an S2 detected without an S1 pulse. They could however be coincidentally seen within a time-window of an isolated S1 pulse mimicking a S1-S2 signal leading to an accidental background. Hotspots originate from the cathode, anode and gate which contain regions of small field perturbations as a result of minor damage and dust build-up resulting in field emission of electrons, thus isolated S2s. Hotspots are not a continuous background but rather sporadic in nature; due to their origins from the HV grids it follows that periods of time with where hotspots are observed could be observed as a signal in the loop antenna over the same time period.

Figure 28 highlights that a prominent hotspot period in LZ, around a month in length, cannot be distinguished by the fast sensors from any other time periods.

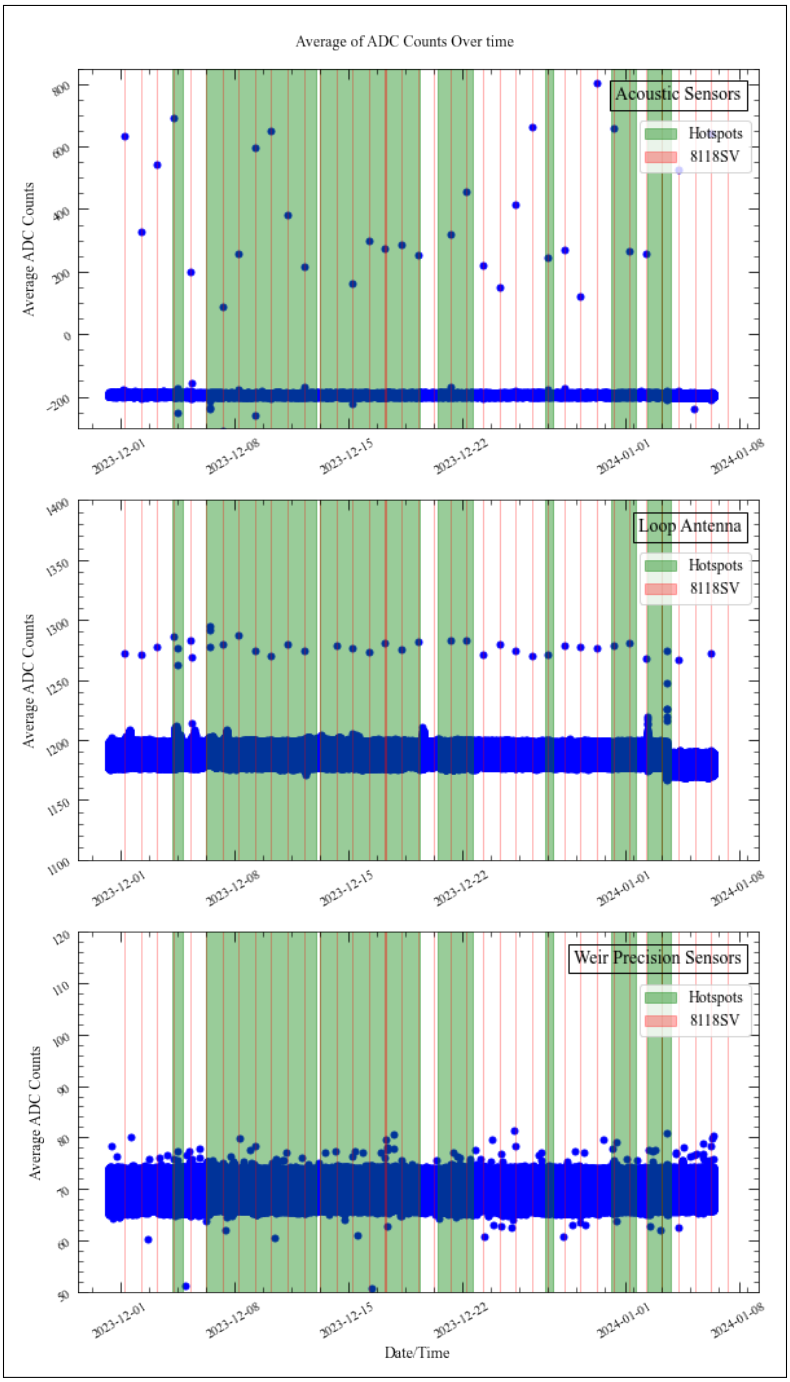


Figure 28: Plot of average ADC count for each fast sensor over December 2023. Periods of hotspots are highlighted in green. There is no clear correlation between any signal in the sensors and periods when hotspots are present.

4.4 LZ as a Seisometer

The LZ detector could be used as a seisometer due to the high accuracy and precision of the internal monitoring sensors as well as the highly sensitive nature of the detector in general. There have been a few small earthquakes in South Dakota since the commissioning of LZ, therefore a study into the monitoring sensors can either confirm that Earthquakes can be observed, or, set a lower-bound for Earthquake magnitudes that could be observed. The largest Earthquake observed surrounding SURF, South Dakota since the commissioning of LZ, according to [36] was a 3.7 on the Richter scale in May 2024, with the epicenter 200miles away from the SURF, where LZ is based. Looking at the sensor data during this time period, as shown in Figure 29 shows that the earthquake is not distinct in the fast sensors, setting a lower-bound of the possible Earthquakes to be seen at 3.7 in magnitude, 200 miles from the epicenter. Other smaller Earthquakes in South Dakota and surrounding states were also explored in the data but none of these were seen in the fast sensors either.

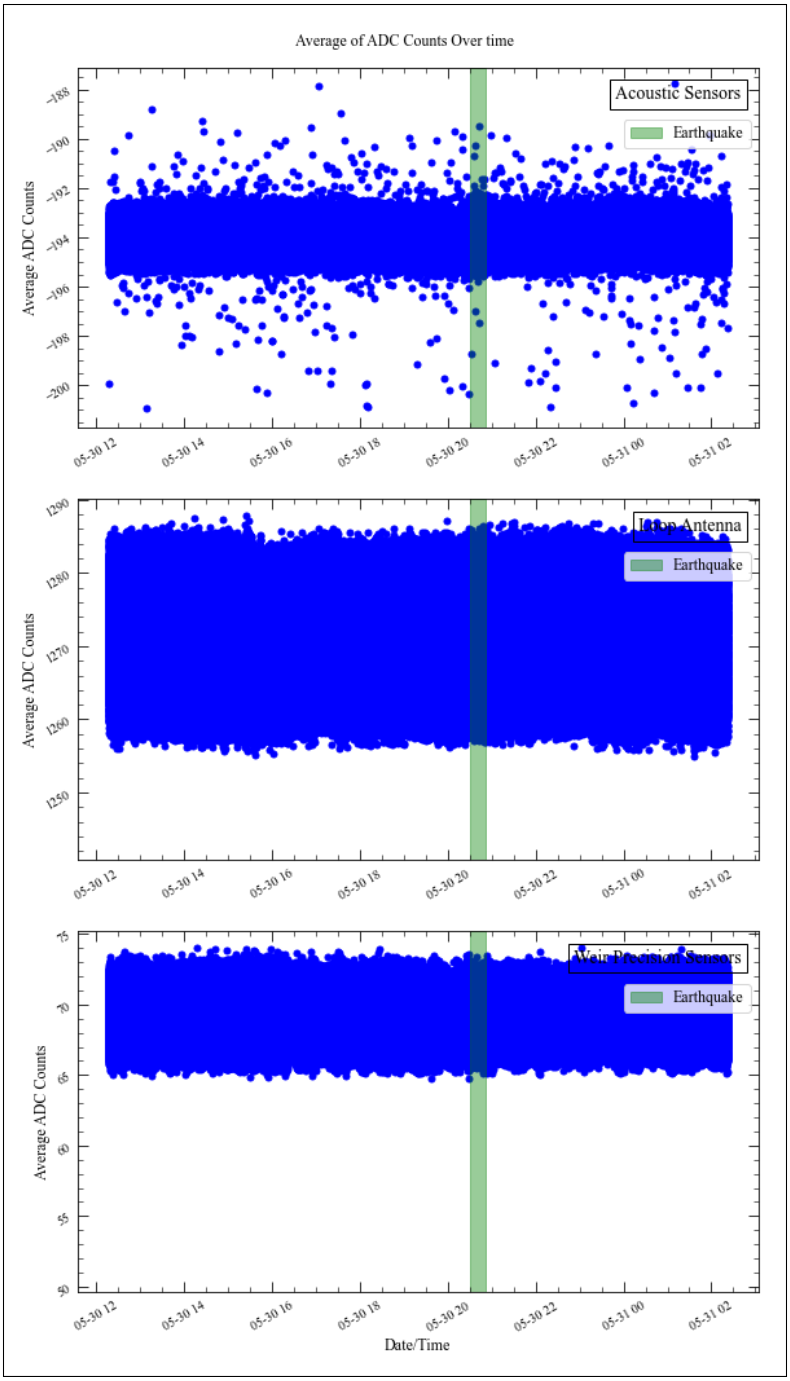


Figure 29: Plot of average ADC count for each fast sensor over around the end of May 2024. A 3.7 magnitude Earthquake is highlighted in green; this is not seen by the fast sensors.

4.5 PMT-Trips

In order to prevent damage to the PMTs a maximum current value is set, if this condition is met or exceeded the voltage in the PMT switches off. This condition could be met due to a variety of conditions, namely, too much light, the gain being set too high or possibly mechanical imperfections in the PMT. Due to the LA's close proximity to the PMTs, it is possible that PMT trips could be seen in the LA. Additionally, one of the LA's design goals was to quickly notify slow control users if a discharge from the HV grids is occurring so that the voltage can be decreased before permanent damage occurs. It is therefore interesting to explore whether recent PMT trips in the LZ detector can be linked to signals observed in the LA, even if they were not caused from HV discharges.

Figures 30 and 31 highlight PMT trips over a period of a few months - there is not anything distinct during the times leading up to and after a PMT trip.

4.6 Conclusion

The signals observed in the AS and LA are well characterised and understood through solenoid valve actuations in the detector and have been linked to increased S1 threshold-crossing rates in the PMTs. This is an important observation for LZ and future liquid noble dark matter detectors as it shows there is value in high frequency sampling of internal monitoring sensors, with the potential for greater value if the sensors were given their own triggering system. Although, so far, the internal monitoring sensors of LZ have had the their main value and purpose related to low frequency sampling for the operations of the experiment, there is future scope for the sensors to be able to veto PMT events based upon the detectors internal conditions during the events. This would be an extremely valuable endeavor for understanding backgrounds in future, larger liquid noble detectors such as XLZD, and it is useful to know that it is possible from this work.

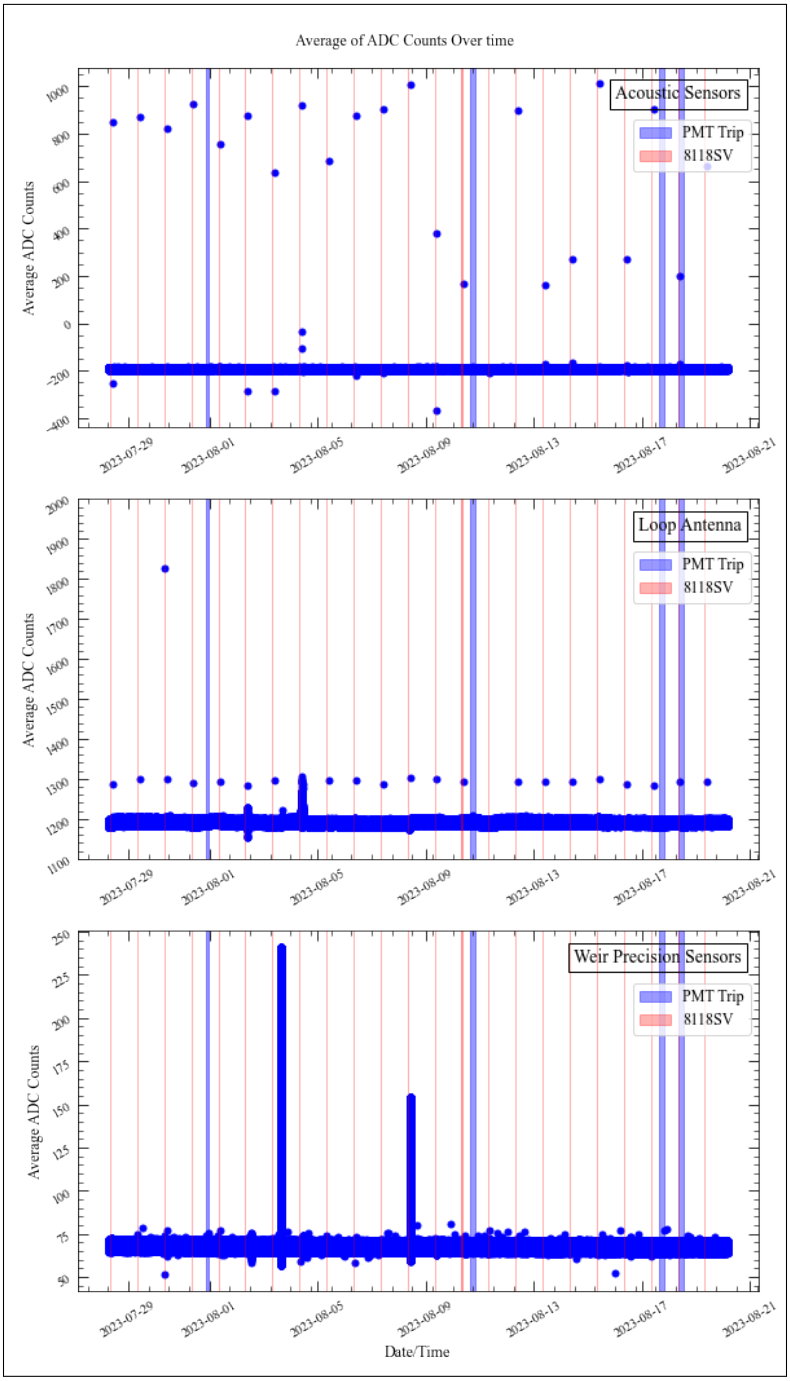


Figure 30: Plot of average ADC count for each fast sensor over August 2023. Times when PMTs are tripped are highlighted in blue. There is no clear correlation between any signal in the sensors and times when PMTs are tripped. The large spikes seen in the WPS are from a power outage and a change of circulation compressors respectively.

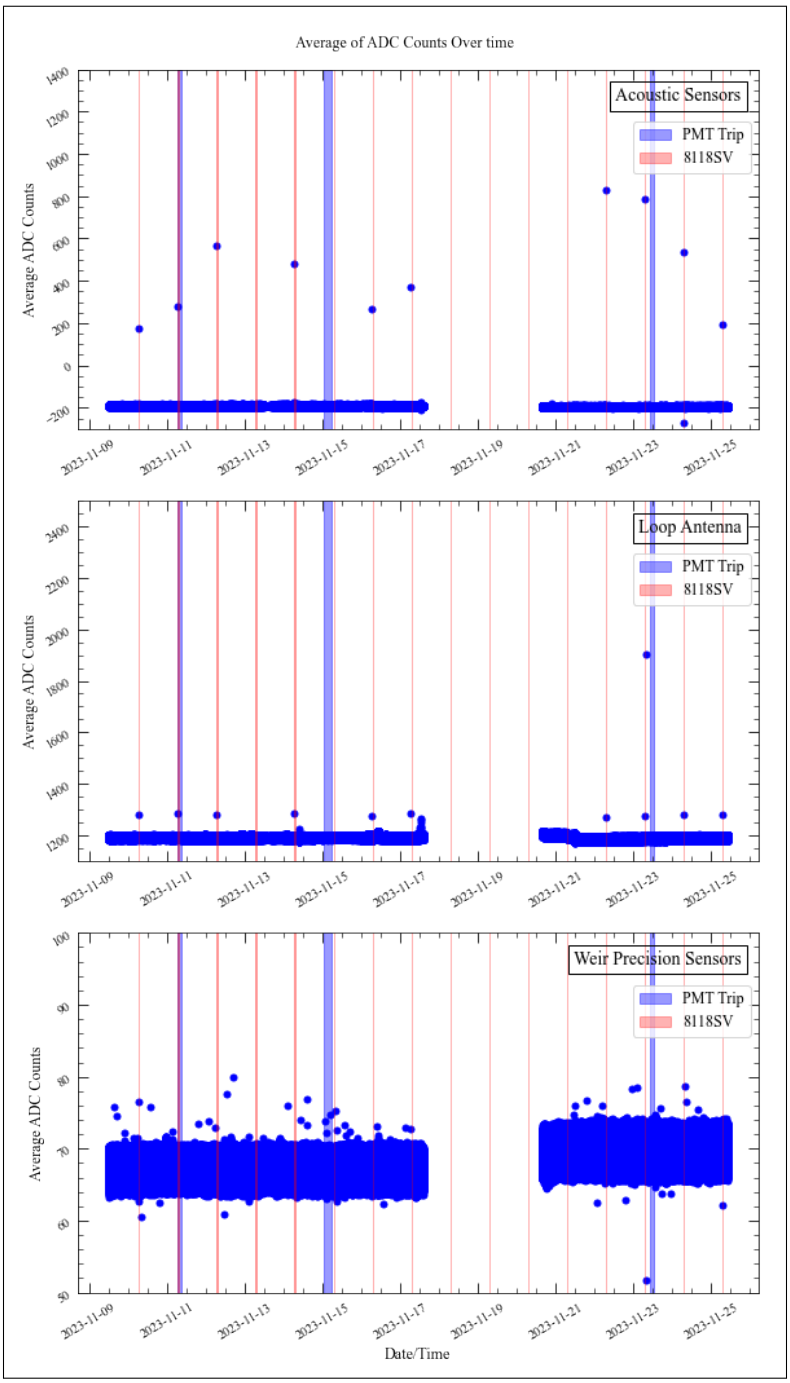


Figure 31: Plot of average ADC count for each fast sensor over November 2023. Times when PMTs are tripped are highlighted in blue. There is no clear correlation between any signal in the sensors and times when PMTs are tripped. The large gap in the data is from a power-outage at the SURF site, it is noted the liquid level height was different after the outage compared to before; this level change is less than 0.1mm and is due to insufficient control over the liquid level.

5 Outlook

Presented above are initial studies into the fast control monitoring sensors data triggered on event. The studies have been successful in creating a framework to make the fast sensor data more accessible to the collaboration, as well as showing that there is useful substance to the data.

The signals observed in the AS and LA are well characterised and understood through solenoid valve actuations in the detector and have been linked to increased S1 threshold-crossing rates in the PMTs; fulfilling a design purpose of the fast sensors by linking signals in the sensors to observed backgrounds in the PMTs.

Periods of hotspot activity, earthquakes and PMT-trips did not see any correlation to signals observed in the sensors. Further work is required to find the origin of the signals seen in the WPS, although it is almost certain these are not from physical changes in the liquid level.

Whilst most signals observed above are characterised, or have started to be understood; data is only collected on PMT triggers. In order to fully understand the fast sensors and thus the detector further, the fast sensors should have their own triggering system in order not to miss signals that are not coincident in the PMT trigger window.

There are many avenues for further exploration and analysis between the fast sensors, signals seen in the PMTs, and changes in detector environment which should be investigated, particularly: recalibrating the WPS and finding the origin behind the signals observed from the two WPS sensors as well as introducing triggers to the fast sensors.

For future liquid noble detectors, such as XLZD, I would recommend that from the outset of the experiment that consideration be given to implementing a dedicated triggering system for the internal sensors that is separate from the PMT system, this would allow an even greater understanding of the detectors internal environment and allow further exploration of the possibility of using the internal sensors to veto events. Additionally, it is important that calibration methods for the internal sensors can be performed after the detector has been commissioned - this is crucial given the increasing duration of data-taking periods in Particle Physics; current fast-sensor calibrations in LZ were

performed in 2019/2020 and are ever-increasingly difficult to validate and re-calibrate as time passes.

References

[1] K. Begeman, A. Broeils, and R. Sanders, "Extended rotation curves of spiral galaxies: Dark haloes and modified dynamics," *Monthly Notices of the Royal Astronomical Society*, vol. 249, no. 3, pp. 523–537, 1991.

[2] N. Aghanim, Y. Akrami, M. Ashdown, J. Aumont, C. Baccigalupi, *et al.*, "Planck2018 results: Vi. cosmological parameters," *Astronomy amp; Astrophysics*, vol. 641, p. A6, Sept. 2020.

[3] "HowToMakeAPlot." https://github.com/cajohare/HowToMakeAPlot/blob/main/plots/DMLandscape_Palatino.pdfhtml. Date Accessed: 21/06/2024.

[4] Y. Meng, Z. Wang, Y. Tao, A. Abdukerim, Z. Bo, W. Chen, X. Chen, Y. Chen, C. Cheng, Y. Cheng, *et al.*, "Dark matter search results from the pandax-4t commissioning run," *Physical Review Letters*, vol. 127, no. 26, p. 261802, 2021.

[5] E. Aprile, K. Abe, F. Agostini, S. Ahmed Maouloud, *et al.*, "First dark matter search with nuclear recoils from the xenonnt experiment," *Phys. Rev. Lett.*, vol. 131, p. 041003, Jul 2023.

[6] D. Akerib, S. Alsum, H. Araújo, X. Bai, A. Bailey, J. Balajthy, P. Beltrame, E. Bernard, A. Bernstein, T. Biesiadzinski, *et al.*, "Results from a search for dark matter in the complete lux exposure," *Physical review letters*, vol. 118, no. 2, p. 021303, 2017.

[7] R. Ajaj, P.-A. Amaudruz, G. Araujo, M. Baldwin, M. Batygov, B. Beltran, C. Bina, J. Bonatt, M. Boulay, B. Broerman, *et al.*, "Search for dark matter with a 231-day exposure of liquid argon using deap-3600 at snolab," *Physical Review D*, vol. 100, no. 2, p. 022004, 2019.

[8] T. L.-Z. Collaboration, "First dark matter search results from the lux-zeplin (lz) experiment," *Physical Review Letters*, vol. 131, July 2023.

[9] D. Akerib, C. Akerlof, A. Alqahtani, S. Alsum, T. Anderson, N. Angelides, H. Araújo, J. Armstrong, M. Arthurs, X. Bai, *et al.*, "Simulations of events for the lux-zeplin (lz) dark matter experiment," *Astroparticle Physics*, vol. 125, p. 102480, 2021.

[10] R. Linehan, R. Mannino, A. Fan, C. Ignarra, S. Luitz, K. Skarpaas, T. Shutt, D. Akerib, S. Alsum, T. Anderson, H. Araújo, *et al.*, "Design and production of the high voltage electrode grids and electron extraction region for the lz dual-phase xenon time projection chamber," *Nuclear Instruments and Methods in Physics Research Section A: Accelerators, Spectrometers, Detectors and Associated Equipment*, vol. 1031, p. 165955, May 2022.

[11] D. Akerib, C. Akerlof, D. Y. Akimov, A. Alquahtani, S. Alsum, T. Anderson, N. Angelides, H. Araújo, A. Arbuckle, J. Armstrong, *et al.*, "The lux-zeplin (lz) experiment," *Nuclear Instruments and Methods in Physics Research Section A: Accelerators, Spectrometers, Detectors and Associated Equipment*, vol. 953, p. 163047, 2020.

[12] T. M. A. Fruth, *PMT studies and loop antenna development for the LZ dark matter experiment*. PhD thesis, University of Oxford, 2019.

[13] F. Liao, *Development of xenon level instrumentation for the LZ dark matter detector*. PhD thesis, University of Oxford, 2017.

[14] R. S. Shankland, "Michelson-Morley Experiment," *American Journal of Physics*, vol. 32, pp. 16–35, 01 1964.

[15] P. A. Ade, N. Aghanim, M. Arnaud, M. Ashdown, J. Aumont, C. Baccigalupi, A. Banday, R. Barreiro, J. Bartlett, N. Bartolo, *et al.*, "Planck 2015 results-xiii. cosmological parameters," *Astronomy & Astrophysics*, vol. 594, p. A13, 2016.

[16] E. Komatsu, J. Dunkley, M. Nolta, C. Bennett, B. Gold, G. Hinshaw, N. Jarosik, D. Larson, M. Limon, L. Page, *et al.*, "Five-year wilkinson microwave anisotropy probe* observations: cosmological interpretation," *The Astrophysical Journal Supplement Series*, vol. 180, no. 2, p. 330, 2009.

[17] F. Zwicky, "On the masses of nebulae and of clusters of nebulae," in *A Source Book in Astronomy and Astrophysics, 1900–1975*, pp. 729–737, Harvard University Press, 1979.

[18] G. Bertone, D. Hooper, and J. Silk, "Particle dark matter: Evidence, candidates and constraints," *Physics reports*, vol. 405, no. 5-6, pp. 279–390, 2005.

[19] W. De Blok, F. Walter, E. Brinks, C. Trachternach, S. Oh, and R. C. Kennicutt, "High-resolution rotation curves and galaxy mass models from things," *The Astronomical Journal*, vol. 136, no. 6, p. 2648, 2008.

[20] M. Bartelmann and P. Schneider, "Weak gravitational lensing," *Physics Reports*, vol. 340, no. 4-5, pp. 291–472, 2001.

[21] D. Clowe, M. Bradač, A. H. Gonzalez, M. Markevitch, S. W. Randall, C. Jones, and D. Zaritsky, "A direct empirical proof of the existence of dark matter," *The Astrophysical Journal*, vol. 648, p. L109–L113, Aug. 2006.

[22] C. L. Bennett, D. Larson, J. L. Weiland, N. Jarosik, G. Hinshaw, N. Odegard, K. Smith, R. Hill, B. Gold, M. Halpern, *et al.*, "Nine-year wilkinson microwave anisotropy probe (wmap) observations: final maps and results," *The Astrophysical Journal Supplement Series*, vol. 208, no. 2, p. 20, 2013.

[23] D. J. Eisenstein, I. Zehavi, D. W. Hogg, *et al.*, "Detection of the baryon acoustic peak in the large-scale correlation function of sdss luminous red galaxies," *The Astrophysical Journal*, vol. 633, p. 560–574, Nov. 2005.

[24] N. Aghanim, Y. Akrami, M. Ashdown, J. Aumont, C. Baccigalupi, M. Ballardini, A. J. Banday, R. Barreiro, N. Bartolo, S. Basak, *et al.*, "Planck 2018 results-vi. cosmological parameters," *Astronomy & Astrophysics*, vol. 641, p. A6, 2020.

[25] P. D. Group, P. A. Zyla, R. M. Barnett, J. Beringer, O. Dahl, *et al.*, "Review of Particle Physics," *Progress of Theoretical and Experimental Physics*, vol. 2020, p. 083C01, 08 2020.

[26] P. Murdin, *Encyclopedia of astronomy & astrophysics*. CRC Press, 2001.

[27] S. P. MARTIN, *A SUPERSYMMETRY PRIMER*, p. 1–98. WORLD SCIENTIFIC, July 1998.

[28] J. L. Feng, "Dark matter candidates from particle physics and methods of detection," *Annual Review of Astronomy and Astrophysics*, vol. 48, no. 1, pp. 495–545, 2010.

[29] L. Bergström, "Non-baryonic dark matter: observational evidence and detection methods," *Reports on Progress in Physics*, vol. 63, p. 793–841, Apr. 2000.

[30] G. Bertone and D. Hooper, "History of dark matter," *Reviews of Modern Physics*, vol. 90, no. 4, p. 045002, 2018.

[31] L. D. Duffy and K. Van Bibber, "Axions as dark matter particles," *New Journal of Physics*, vol. 11, no. 10, p. 105008, 2009.

[32] T. L.-Z. Collaboration, "Lux-zeplin (lz) technical design report," tech. rep., Argonne National Lab.(ANL), Argonne, IL (United States); Pacific Northwest ..., 2017.

[33] E. Aprile and T. Doke, "Liquid xenon detectors for particle physics and astrophysics," *Reviews of Modern Physics*, vol. 82, no. 3, pp. 2053–2097, 2010.

[34] A. Zani *et al.*, "The darkside-20k experiment," *Journal of Instrumentation*, vol. 19, no. 03, p. C03058, 2024.

[35] C. Zhang and D.-M. Mei, "Evaluation of cosmogenic production of 39ar and 42ar for rare-event physics using underground argon," *Astroparticle Physics*, vol. 142, p. 102733, 2022.

[36] "United States Geological Survey." https://www.usgs.gov/programs/earthquake-hazards. Date Accessed: 13/08/2024.